

# Tracing stars in Milky Way satellites with A-SLOTH

Li-Hsin Chen<sup>1,2</sup>, Mattis Magg<sup>1,2</sup>, Tilman Hartwig<sup>3,4,5</sup>, Simon C. O. Glover<sup>1</sup>,  
Alexander P. Ji<sup>7,8</sup> and Ralf S. Klessen<sup>1,6</sup>

<sup>1</sup>Universität Heidelberg, Zentrum für Astronomie, Institut für Theoretische Astrophysik, D-69120 Heidelberg, Germany

<sup>2</sup>International Max Planck Research School for Astronomy and Cosmic Physics at the University of Heidelberg (IMPRS-HD)

<sup>3</sup>Department of Physics, School of Science, The University of Tokyo, Bunkyo, Tokyo 113-0033, Japan

<sup>4</sup>Institute for Physics of Intelligence, School of Science, The University of Tokyo, Bunkyo, Tokyo 113-0033, Japan

<sup>5</sup>Kavli Institute for the Physics and Mathematics of the Universe (WPI), The University of Tokyo Institutes for Advanced Study,

<sup>6</sup>Universität Heidelberg, Interdisziplinäres Zentrum für Wissenschaftliches Rechnen, D-69120 Heidelberg, Germany

<sup>7</sup>Department of Astronomy & Astrophysics, University of Chicago, 5640 S Ellis Avenue, Chicago, IL 60637, USA

<sup>8</sup>Kavli Institute for Cosmological Physics, University of Chicago, Chicago, IL 60637, USA

## ABSTRACT

We study the stellar mass-to-halo mass relation at  $z = 0$  in 30 Milky Way-like systems down to the ultra-faint ( $M_* < 10^5 M_\odot$ ) regime using the semi-analytic model A-SLOTH. A new model allows us to follow star formation and the stochastic stellar feedback from individually sampled Pop II stars. Our fiducial model produces consistent results with the stellar mass-to-halo mass relation derived from abundance matching and the observed cumulative stellar mass function above the observational completeness. We find a plateau in the stellar mass-to-halo mass relation in the ultra-faint regime. The stellar mass of this plateau tells us how many stars formed before supernovae occur and regulate further star formation, which is determined by the Pop II star formation efficiency. We also find that the number of luminous satellites increases rapidly as  $M_*$  decreases until  $M_* \approx 10^4 M_\odot$ . Finally, we find that the relative streaming velocity between baryons and dark matter at high redshift is important in determining the number of ultra-faint dwarf galaxies at  $z = 0$ . The new model in A-SLOTH provides a framework to study the stellar properties and the formation history of metal-poor stars in Milky Way and its satellites.

**Key words:** methods: numerical – galaxies: star formation – galaxies: dwarf – stars: Population II – stars: Population III

## 1 INTRODUCTION

Galaxy formation depends heavily on properties and evolution of the host dark matter halo. The most straightforward connection between them is perhaps the stellar mass-to-halo mass (SMHM) relation. Previous studies have found that for systems with stellar masses  $M_* > 10^5 M_\odot$  (Drlica-Wagner et al. 2020; Garrison-Kimmel et al. 2014, 2017; Jethwa et al. 2018; Nadler et al. 2020), the galaxies and their host haloes follow a tight SMHM relation. However, whether this relation still holds for ultra-faint dwarf galaxies ( $M_* < 10^5 M_\odot$ , UFDs) is still unclear. In recent years, numerous UFDs around the Milky Way (MW) have been discovered by large surveys (Willman 2010; Drlica-Wagner et al. 2015, 2020; Koposov et al. 2015; Torrealba et al. 2016, 2018). Despite the low completeness of UFD discoveries, these UFDs already provide us with constraints on the SMHM relation and the underlying galaxy formation model.

There have been many recent cosmological zoom-in simulations of MW-like systems or isolated UFDs (e.g. Hop-

kins et al. 2014; Wetzel et al. 2016; Wheeler et al. 2019; Libeskind et al. 2020; Font et al. 2020, 2021; Engler et al. 2021). These simulations still cannot resolve the smallest dwarf galaxies in the MW system. Due to the high spatial and mass resolutions that are needed to properly simulate UFDs, the required time and computational resource is immense. Semi-analytic models provide an opportunity to explore different physical processes and a wider range of parameters. For example, de Bannassuti et al. (2014, 2017) utilized the semi-analytic code GAMETE to investigate the metallicity distribution function in the Galactic halo and the carbon-enhanced metal-poor stars. Their model is based on the Extended Press–Schechter formalism (Press & Schechter 1974; Lacey & Cole 1993) and includes the transition between metal-free and metal-enriched star formation following metal and dust evolution. Salvadori et al. (2015) and Rossi et al. (2021) employed GAMETE to study the carbon-enhanced metal-poor stars in the dwarf galaxies in the Local Group. Visbal et al. (2018, 2020) studied the metal-free

star formation rate down to  $z = 6$ , including physical processes such as photo-ionization, Lyman-Werner (LW) radiation, and metal enrichment. Kravtsov & Manwadkar (2021) used GRUMPY to study the stellar mass-to-halo mass relation and stellar mass-metallicity relations in the dwarf galaxies. However, they do not include metal-free star formation in their model.

In this work, we use our semi-analytic galaxy formation code A-SLOTH (Ancient Stars and Local Observables by Tracing haloes, Magg et al. in prep) to study the SMHM relation in satellites of MW-like systems. A-SLOTH has been used to study various problems, such as the lower limit of initial mass function (IMF) of metal-free stars (Hartwig et al. 2015), the connection between the metal-poor stars in the MW and their progenitors (Hartwig et al. 2018, 2019), the probability of finding metal-free survivors in the MW (Magg et al. 2018), and the inhomogeneous mixing of metals in the interstellar medium (Tarumi et al. 2020). In these previous studies, A-SLOTH only tracked the total mass of metal-enriched stars forming in each system, rather than tracing the formation and evolution of the stars individually. Therefore, the corresponding stellar feedback was considered to be continuous and computed using IMF-averaged quantities. In this paper, we introduce a new model in A-SLOTH that allows metal-enriched stars to be traced individually. This enables A-SLOTH to properly follow the detailed star formation activity in individual systems and the impact of stellar feedback. We describe the general structure and the star formation models of metal-free and metal-enriched stars in Section 2. We describe how we calibrate the free parameters in our model in Section 3. We discuss the main results in Section 4. We discuss the implications of our new model and results in Section 5. Finally, we summarize this work in Section 6.

## 2 NUMERICAL METHOD

A complete description of the physical processes accounted for in A-SLOTH is given in Magg et al. (in prep). Here, we focus on the parts of the model that are the most important for our current study.

### 2.1 Merger trees

A-SLOTH uses dark matter halo merger trees drawn from the *Caterpillar* project (Griffen et al. 2016), which is a dark-matter-only cosmological simulation suite focusing on the assembly of MW-sized haloes and their satellite galaxies. It is based on the Planck Collaboration et al. (2014) cosmological parameters in a  $100 h^{-1}\text{Mpc}$  box. MW-like systems are selected at  $z = 0$  if the main haloes fulfill the following criteria:

- (i) Virial mass in range  $0.7 \times 10^{12} M_{\odot} \leq M_{\text{vir,peak}} \leq 3 \times 10^{12} M_{\odot}$ .
- (ii) There is no halo with  $M_{\text{vir,peak}} \geq 7 \times 10^{13} M_{\odot}$  within 7 Mpc.
- (iii) There are no other haloes with  $M_{\text{vir,peak}} \geq 0.5 \times M_{\text{main}}$  within 2.8 Mpc of the main halo.

Dark matter haloes are identified with ROCKSTAR (Behroozi et al. 2013) and  $M_{\text{vir,peak}}$  is the maximum virial

mass along the main branch a halo ever attains up to the current redshift, that is computed with the evolution of the virial relation from Bryan & Norman (1998). We adopt their notation here. Griffen et al. (2016) extracted the full merger history of these MW-like systems, including dark matter and spatial information of the haloes and global time-steps between the snapshots,  $\Delta t_z$ , which is  $\approx 5\text{Myr}$  down to  $z = 6$  and  $\approx 50\text{Myr}$  at  $z = 6 - 0$ . In this work, we select 30 merger trees from their sample. A-SLOTH walks through these merger trees and determines the baryonic contents of each halo in the merger tree based on the implemented physics. We describe the physical processes in the following sections.

### 2.2 Population III (Pop III) stars

We follow the same metal-free (Pop III) star formation (SF) model as in our previous works (Magg et al. 2018; Tarumi et al. 2020). We briefly summarize the model here. Pop III stars are assumed to form when  $\text{H}_2$  can cool primordial gas efficiently, which means that a halo needs to exceed a critical mass,  $M_{\text{crit}}$ . In A-SLOTH, Pop III stars form instantly in a single star burst in a mini-halo (haloes below the atomic cooling threshold ( $T_{\text{vir}} = 10000\text{K}$ ) as soon as its virial mass exceeds  $M_{\text{crit}}$ . By default, we follow the prescriptions given in Schauer et al. (2021, their Eqs. 9 and 10) and Hummel et al. (2012, their Eq. 1) to determine  $M_{\text{crit}}$ . Schauer et al. (2021) showed that the critical mass is dependent on the LW background and the large-scale streaming velocity of the baryons relative to the dark matter:

$$\log_{10} M_{\text{crit,S21}} = 6.0174 (1.0 + 0.166\sqrt{J_{21}}) + 0.4159 \frac{v_{\text{BC}}}{\sigma_{\text{rms}}}. \quad (1)$$

Here,  $M_{\text{crit,S21}}$  is the critical mass in units of solar masses,  $J_{21}$  is the strength of LW background in units of  $10^{-21} \text{erg s}^{-1} \text{cm}^{-2} \text{Hz}^{-1} \text{sr}^{-1}$ ,  $v_{\text{BC}}$  is the large-scale streaming velocity of the baryons relative to the dark matter in units of  $\sigma_{\text{rms}}$ , and  $\sigma_{\text{rms}}$  is the root-mean-squared value of the streaming velocity. We denote this default model hereafter as S21. We do not self-consistently follow the build-up of the LW background, because the effective volume of our MW-like merger trees is too small to obtain a cosmologically representative estimate of the LW background. Instead, we adopt the simple redshift-dependent fitting formula,

$$J_{21} = 10^{2-z/5}, \quad (2)$$

which is based on the work in Greif & Bromm (2006). We take  $v_{\text{BC}} = 0.8\sigma_{\text{rms}}$  as the fiducial baryonic streaming velocity, since this is the most likely value to be present at a randomly selected point in the Universe (Schauer et al. 2021). The impact of varying our treatment of both of these effects is explored in Section 4.2.

In addition, we assume that gas can cool down efficiently and form stars in haloes that have virial temperatures above the atomic cooling limit ( $T_{\text{vir}} \geq 10^4\text{K}$ ) when there is no strong ionizing radiation field (Visbal et al. 2017). Therefore, we consider haloes that have virial masses larger than  $M_{\text{crit},10^4\text{K}}$  can form Pop III stars, where  $M_{\text{crit},10^4\text{K}}$  is computed by

$$M_{\text{crit},10^4\text{K}} = 10^7 \left( \frac{1+z}{10} \right)^{-1.5}. \quad (3)$$

The final critical mass is then determined by  $M_{\text{crit,fin}} = \text{MIN}(M_{\text{crit,S21}}, M_{\text{crit},10^4\text{K}})$ .

Cold gas is converted to Pop III stars in haloes with  $M_{\text{halo}} \geq M_{\text{crit}}$  at a fixed efficiency  $\eta_{\text{III}}$ , defined such that  $M_{*,\text{III}} = \eta_{\text{III}}\Omega_{\text{b}}M_{\text{halo}}/\Omega_{\text{m}}$ , where  $M_{\text{halo}}$  is the current virial mass of the halo,  $\Omega_{\text{b}}$  is the baryon density parameter today, and  $\Omega_{\text{m}}$  is the matter density parameter today. We adopt  $\Omega_{\text{b}} = 0.0486$  and  $\Omega_{\text{m}} = 0.3089$  (Planck Collaboration et al. 2016). We follow the Pop III model in Tarumi et al. (2020) and sample stars stochastically from an IMF with a slope of  $dN/d(\log M) \propto M^{0.5}$  in the mass range of  $2 < M_* < 180M_{\odot}$ . Further SF is halted when the total mass of newly-formed Pop III reaches  $M_{*,\text{III}}$ .

We calculate the stellar lifetimes of Pop III stars by interpolating between values assembled from several previous studies: Marigo et al. (2001) for stars in the mass range  $0.7\text{--}100M_{\odot}$ ; Schaerer (2002) for stars in the mass range  $5\text{--}500M_{\odot}$  (and note that we consider their models without mass loss); and Ekström et al. (2008) for stars in the mass range  $9\text{--}200M_{\odot}$ . If the stellar lifetime of a star is provided by multiple works, we use the mean value. Pop III stars die as core-collapse supernovae (CCSNe) in the range of  $10\text{--}40M_{\odot}$  and as pair-instability supernovae (PISNe) in the range of  $140\text{--}260M_{\odot}$  (Heger & Woosley 2002, 2010). Following Tarumi et al. (2020), we further assume that 30% ( $f_{\text{faint}} = 0.3$ ) of the Pop III CCSNe explode as faint supernovae. We use the tabulated metal yields provided in Kobayashi et al. (2011) and Nomoto et al. (2013) for PISNe and normal CCSNe, and the yields in Ishigaki et al. (2014, 2018) for faint CCSNe. We assume that a fraction  $f_{\text{fallback}} = 0.2$  (Ritter et al. 2015) of the metals remains in the mini-halo after the supernovae have exploded, with the remaining fraction  $(1 - f_{\text{fallback}})$  gaining enough energy from the SNe to escape from the gravitational well of the mini-halo. Tarumi et al. (2020) calibrated the Pop III SF efficiency ( $\eta_{\text{III}}$ ),  $f_{\text{faint}}$  and  $f_{\text{fallback}}$  to reproduce the observed MW metallicity distribution function (MDF). The main focus of this work is on the stellar masses of the dwarf galaxies and our model does not heavily depend on metallicity. Therefore, we adopt the same values of  $\eta_{\text{III}}$ ,  $f_{\text{faint}}$  and  $f_{\text{fallback}}$  as in Tarumi et al. (2020) without investigating the effects of these parameters in detail.

Following the initial Pop III star burst, we assume that any future star formation in the same halo will be in the form of metal-enriched stars. However, stellar feedback will have heated the gas in the mini-halo and ejected a fraction of it. Therefore, further SF is suppressed until the gas re-accumulates and cools down. We denote this time between the Pop III star burst and the onset of further star formation as  $t_{\text{rec}}$ , known as the recovery time, which was calibrated by Tarumi et al. (2020).

### 2.3 Population II (Pop II) stars

In our model, we do not distinguish between metal-rich (Population I) and metal-poor (Population II) stars and classify all metal-enriched stars as Population II (Pop II) stars. We implement an improved Pop II SF model, which is based on the models in Magg et al. (2018) and Tarumi et al. (2020). The explanations of important variables in the Pop II SF model are listed in Table 1. We assume that the baryons initially associated with a given dark matter halo are located either in cold gas ( $M_{\text{cold}}$ ), in hot gas ( $M_{\text{hot}}$ ),

Name	Definition
$M_{\text{vir,peak}}$	peak virial mass of the halo up to current $z$
$M_{\text{cold}}$	cold gas mass
$M_{\text{hot}}$	hot gas mass
$M_{\text{out}}$	cumulative outflow mass
$M_{*,\text{II}}$	total Pop II stellar mass
$M_{\text{disk}}$	disk mass, including gas and stars
$\delta M_{\text{out}}$	outflow mass
$\delta M_{\text{out,cold}}$	cold gas mass that enters outflow
$\delta M_{\text{out,hot}}$	hot gas mass that enters outflow
$\delta M_{\text{heat}}$	mass that transfers from cold gas to hot gas
$\delta M_{*,\text{II}}$	Pop II stellar mass that is formed
$\delta M_{\text{acc,hot}}$	hot gas mass that is accreted from IGM
$i$	step $i$ in the subcycle
$n_{\text{bins,II}}$	number of Pop II IMF bins
$M_{\text{bound,II}}$	lower and upper limits of Pop II stellar mass
$n_{\text{cold}}^{\text{den}}$	number density of dense gas
$v_{\text{BC}}$	relative streaming velocity between baryon and dark matter
$\eta_{\text{II}}$	Pop II star formation efficiency
$\alpha_{\text{II}}$	slope of the Pop II IMF
$\gamma_{\text{out}}$	outflow efficiency (Eq. 17)
$\alpha_{\text{out}}$	exponent in $\gamma_{\text{out}}$
$M_{\text{norm}}$	normalization mass in $\gamma_{\text{out}}$
$\Delta t_z$	time difference between each snapshot in the merger tree
$\delta t_i$	adaptive time-step $i$ in the SF subcycle
$t_{\text{dyn}}$	dynamical time scale of the halo
$t_{\text{cold,ff}}$	free-fall time scale of cold gas
$t_{\text{star}}$	stellar formation time scale
$t_{\text{cool}}$	cooling time scale
$t_{\text{acc}}$	hot gas accretion time scale

**Table 1.** Definitions of the variables in the Pop II star formation model.

in a Pop II stellar component ( $M_{*,\text{II}}$ ), or have been lost from the halo in an outflow ( $M_{\text{out}}$ ). The initial baryonic mass of a halo with virial mass  $M_{\text{vir,peak}}$  is assumed to be  $(\Omega_{\text{b}}/\Omega_{\text{m}})M_{\text{vir,peak}}$ . Therefore, by construction

$$M_{\text{vir,peak}} \frac{\Omega_{\text{b}}}{\Omega_{\text{m}}} = M_{\text{cold}} + M_{\text{hot}} + M_{*,\text{II}} + M_{\text{out}} \quad (4)$$

is always maintained in the model. Note that in our model, hot gas is any gas that is not cold, i.e. it corresponds to the sum of the warm and hot phases of the ISM in the usual three-phase description (Cowie et al. 1981; Klessen & Glover 2016). We do not account for Pop III stars in the mass budget because the small value we adopt for  $\eta_{\text{III}}$  means that they never represent more than a small fraction of their baryonic mass in any halo. Additionally, they occupy a negligible fraction of the stellar mass at  $z = 0$  and the Pop III stars that remain on the main sequence after  $t_{\text{rec}}$  are too low mass to contribute significantly to the stellar feedback.

Unlike Pop III SF, we assume that Pop II stars can form in multiple epochs, and so we further divide the global time-steps ( $\Delta t_z$ ) from the merger tree into smaller ones. In other words, we have subcycles in our Pop II SF model. The subcycle time-step is denoted as  $\delta t_i$ , and we describe how we determine it in our simulation at the end of this section. A halo is labeled to trigger Pop II SF if the time since it experienced Pop III SF equals or exceeds  $t_{\text{rec}}$  or if it is externally enriched by supernovae from nearby haloes.

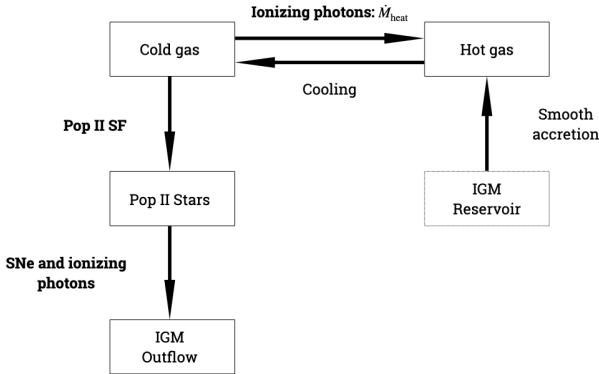


**Figure 1.** Connections between physical processes and baryonic contents in our Pop II SF model.

Prior to the subcycling of Pop II SF, we initialize the halo by inheriting the baryonic contents from all of its progenitors, which gives us  $M_{\text{cold}}^0$ ,  $M_{\text{hot}}^0$ ,  $M_{*,\text{II}}^0$ , and  $M_{\text{out}}^0$ . Then, in time-step  $i$  of the subcycle, the baryonic quantities are updated with the following equations:

$$\begin{aligned} M_{\text{cold}}^{i+1} &= M_{\text{cold}}^i + \frac{\delta t_i M_{\text{hot}}^i}{t_{\text{dyn}}} - \delta M_{\text{out,cold}}^i - \delta M_{\text{heat}}^i - \delta M_{*,\text{II}}^i, \\ M_{\text{hot}}^{i+1} &= M_{\text{hot}}^i - \frac{\delta t_i M_{\text{hot}}^i}{t_{\text{dyn}}} - \delta M_{\text{out,hot}}^i + \delta M_{\text{heat}}^i + \delta M_{\text{acc,hot}}^i, \\ M_{\text{out}}^{i+1} &= M_{\text{out}}^i + \delta M_{\text{out,cold}}^i + \delta M_{\text{out,hot}}^i. \end{aligned} \quad (5)$$

We start from  $i = 0$  and make sure the last time-step in the subcycle always ends exactly at the next global time-step of the merger trees.

There are several physical processes that enter the above equations. We show the connections between these processes and the baryonic contents in our Pop II SF model in Figure 1:

#### (i) Cooling of hot gas

We assume that hot gas cools on a timescale equal to the dynamical time of the stellar disk,  $t_{\text{dyn}}$ . Therefore, during the subcycle time-step  $\delta t_i$ , a mass of gas  $M_{\text{hot}}^i \delta t_i / t_{\text{dyn}}$  is transferred from the hot gas reservoir to the cold gas reservoir.

#### (ii) Heating of cold gas and gas removal by photoionization

We consider the effects of photoionization feedback from massive stars,  $\delta M_{\text{heat}}^i$ . In haloes below the atomic cooling limit ( $T_{\text{vir}} = 10000\text{K}$ ),  $\delta M_{\text{heat}}^i$  is added directly to the outflow, whereas in haloes above the atomic cooling limit, an amount of gas with a mass of  $\delta M_{\text{heat}}^i$  is removed from the cold gas reservoir and added to the hot gas reservoir. The derivation of  $\delta M_{\text{heat}}^i$  is given in Section (i).

#### (iii) Accretion of hot gas

We assume that hot gas is continuously accreted from the

intergalactic medium. In time-step  $i$ , an amount of hot gas

$$\delta M_{\text{acc,hot}}^i = \left( \frac{\Omega_b}{\Omega_m} M_{\text{vir,peak}} - M_{\text{cold}}^0 - M_{\text{hot}}^0 - M_{*,\text{II}}^0 - M_{\text{out}}^0 \right) \frac{\delta t_i}{\Delta t_z}, \quad (6)$$

is added to the hot gas reservoir.

#### (iv) Ejection of hot and cold gas

We account for the loss of both hot and cold gas from the halo due to the effects of stellar feedback, as described in Sections (i) and (ii).

#### (v) Pop II star formation

We assume that Pop II stars form with an IMF given by Kroupa (2001) in the mass range  $0.01 - 100M_{\odot}$ . We sample this IMF using  $4095 + 1$  logarithmically-spaced bins ( $n_{\text{bins,II}} = 4096$ ). Stars with masses  $\leq 0.81M_{\odot}$  have stellar lifetimes larger than the age of universe (Marigo et al. 2001) and they do not contribute significantly to stellar feedback. Therefore, we use only a single mass bin to represent long-lived stars and adopt a finer mass resolution for  $M_{\text{star}} > 0.81M_{\odot}$ .

To estimate how much cold gas is converted into stars during a subcycle time-step, we first calculate

$$M_{*,\text{II,est}}^i = \eta_{\text{II}} M_{\text{cold}}^i \frac{\delta t_i}{t_{\text{cold,ff}}^i}, \quad (7)$$

where  $\eta_{\text{II}}$  is the Pop II SF efficiency,  $t_{\text{cold,ff}}^i = (G\rho_{\text{cold}}^i)^{-1/2}$  is the free-fall time of the cold gas,  $\rho_{\text{cold}}^i = M_{\text{cold}}^i / V_{\text{cold}}$  is the mean cold gas density of the halo,  $M_{\text{cold}}^i$  and  $V_{\text{cold}}$  are the cold gas mass and volume that cold gas occupies, respectively. We assume that the cold gas and stars occupy only the innermost 5% (in radius) of the halo, which is fixed during the subcycle, and so

$$V_{\text{cold}} = \frac{4\pi}{3} (0.05 R_{\text{vir}})^3.$$

Next, we compute the number of stars in each IMF mass bin  $j$  if they follow exactly the Kroupa IMF,  $n_{j,\text{avg}}$ , which can be computed from  $M_{*,\text{II,est}}^i$  by

$$n_{j,\text{avg}} = \frac{C_{\text{II}} m_{j,\text{star}}^{\alpha_{\text{II}}}}{\sum_{j=1}^{N_{\text{bin}}} C_{\text{II}} m_{j,\text{star}}^{\alpha_{\text{II}}+1}} M_{*,\text{II,est}}^i, \quad (8)$$

where  $m_{j,\text{star}}$  is the stellar mass of one star in IMF bin  $j$ ,  $\alpha_{\text{II}}$  is the slope and  $C_{\text{II}}$  is the coefficient:  $C_{\text{II}} = 1$  and  $\alpha_{\text{II}} = 0.7$  in the mass range  $0.08M_{\odot} < m_{j,\text{star}}$ ,  $\alpha_{\text{II}} = -0.3$  and  $C_{\text{II}} = 0.08$  in the mass range  $0.08M_{\odot} \leq m_{j,\text{star}} < 0.5M_{\odot}$ , and  $\alpha_{\text{II}} = -1.3$  and  $C_{\text{II}} = 0.04$  in the mass range  $0.5M_{\odot} \leq m_{j,\text{star}}$  (Kroupa 2001).

We calculate the averaged mass of stars with masses  $< 0.81M_{\odot}$  which leads to  $m_{1,\text{star}} = 0.174M_{\odot}$  and  $n_{1,\text{avg}} = 2.454M_{*,\text{II,est}}^i / M_{\odot}$ . We then compute

$$n_{j,\text{avg}} = \frac{0.573(m_{j,\text{star}})^{-1.3}}{\sum_{j=2}^{4096} (m_{j,\text{star}})^{-0.3}} M_{*,\text{II,est}}^i \quad (9)$$

for stars with masses  $\geq 0.81M_{\odot}$ .

Finally, if  $n_{j,\text{avg}} \leq 10$ , we randomly generate a number,  $n_{j,\text{poi}}$  of stars via Poisson sampling. Poisson sampling has the advantage that with a constant SF rate, we can still form the correct number of stars over a time-period even if the time-steps are so small that far less than one star



forms per sub-time-step (Sormani et al. 2017). We deactivate the Poisson sampling if  $n_{j,\text{avg}} > 10$  and use  $n_{j,\text{avg}}$  directly because Poisson sampling is computationally expensive and the difference between  $n_{j,\text{avg}}$  and  $n_{j,\text{poi}}$  when  $n_{j,\text{avg}} > 10$  is small. The total mass of newly formed Pop II stars in each step  $i$  is then  $\delta M_{*,\text{II}}^i = \Sigma m_{j,\text{star}} n_j$ , where  $n_j$  is the number of stars in bin  $j$ . Throughout the simulation, we track massive stars ( $> 8M_\odot$ ) individually because their stellar feedback is important to subsequent SF. We adopt  $\eta_{\text{II}} = 2$  as our fiducial value and explain the calibration in Section 3.

Finally, we adopt adaptive time-steps in the subcycles, which means that  $\delta t_i$  varies. The adaptive time-step guarantees that all physical processes are accurately resolved when the relative change in any component of the baryonic mass budget is fast, and that we save computational time where the relative change is slow. We calculate three additional timescales:

$$\begin{aligned} t_{\text{star}} &= \frac{M_{*,\text{II}}}{M_{\text{cold}}} t_{\text{cold,ff}}, \\ t_{\text{cool}} &= \frac{M_{\text{cold}}}{M_{\text{hot}}} t_{\text{dyn}}, \\ t_{\text{acc}} &= \frac{M_{\text{hot}}}{\frac{\Omega_{\text{b}}}{\Omega_{\text{m}}} M_{\text{vir,peak}} - (M_{\text{cold}}^0 + M_{\text{hot}}^0 + M_{*,\text{II}}^0 + M_{\text{out}}^0)} \Delta t_z. \end{aligned} \quad (10)$$

Using these, we set the sub-cycle time-step following:

$$\delta t_i = 0.25 \min(t_{\text{star}}, t_{\text{cold}}, t_{\text{acc}}, t_{\text{dyn}}, \Delta t_z). \quad (11)$$

We then shorten the sub-cycle time-step, if necessary, to ensure that we do not overshoot the end of the current redshift step,  $\Delta t_z$ . Our use of adaptive time-steps for the sub-cycles guarantees that mechanical and radiative feedback are sufficiently resolved in time, but significantly reduces the computational cost compared to what would be required using a small fixed time-step.

## 2.4 Stellar Feedback from Pop II stars

During their stellar lifetime, massive stars ( $> 8M_\odot$ ) emit copious amount of ionizing photons. Furthermore, stars with masses in the range  $10 - 40M_\odot$  die as CCSNe (Heger & Woosley 2002, 2010). Each CCSN produces an amount of energy  $E_{\text{SN}} = 10^{51}$  erg and the energy is injected into the interstellar medium (ISM). Here we describe how the photons emitted by massive stars and the energy from SNe affect the ISM in our model.

### (i) Photoheating

The ionizing photons heat up the dense cold gas surrounding the star forming region. For stars with different masses, we calculate a time-averaged mass conversion rate,  $\dot{M}_{\text{heat}}$ , over their lifetimes. We first calculate the instantaneous mass conversion rate by

$$\dot{M}_{\text{heat}} = 10^{-25} m_{\text{H}} n_{\text{cold}}^{\text{den}} R_{\text{D}}^2 c_s \left[ 1 + \frac{7}{4} \frac{c_s (t - t_{\text{D}})}{R_{\text{D}}} \right]^{-1/7} [M_\odot \text{yr}^{-1}], \quad (12)$$

where  $m_{\text{H}} = 1.66 \times 10^{-24}$  g is the mass of a hydrogen atom,  $n_{\text{cold}}^{\text{den}} = 10^3 \text{ cm}^{-3}$  is the number density,  $c_{\text{s,ion}} = 11.4 (T_{\text{ion}}/10^4)^{1/2} \times 10^5 \text{ cm/s}$  is the sound speed, and  $T_{\text{ion}} =$

$10^4 \text{ K}$  is the temperature of the ionized gas. We denote the distance between the ionizing front and the star, and the time it takes when the I-front reaches D-type expansion, as  $R_{\text{D}}$  and  $t_{\text{D}}$ , respectively. The full derivation of Eq. 12 is in Appendix B1.

We note that  $R_{\text{D}}^2$ ,  $t_{\text{D}}$  and therefore  $\dot{M}_{\text{heat}}$  show a non-linear behavior with the ionizing photon emission rate. Stars that form in a cluster are less efficient at heating their ambient medium than isolated stars. Since there is no spatial information inside the halo available from the *Caterpillar* trees, we assume that 90% of the massive stars form in the very central region of the halo that can be considered as one big star cluster. We add the ionizing photons from these 90% of massive stars and calculate one  $\dot{M}_{\text{heat,cl}}$ . For the rest of massive stars (10%), we assume that they form in isolation and calculate a  $\dot{M}_{\text{heat,iso}}$  for each of them. In time-step  $i$ , we sum up the contributions from all of the massive stars to calculate the mass that is converted from cold phase to hot phase,

$$\delta M_{\text{heat},i} = \left( \dot{M}_{\text{heat,cl}} + \Sigma_{j=1}^N \overline{\dot{M}_{\text{heat,iso}}^j} \right) \delta t_i. \quad (13)$$

We examine two extreme cases: 1) all massive stars form in isolation and 2) all massive stars reside in one big star cluster and show the results in Appendix C.

In mini-haloes with  $T_{\text{vir}} < 10000 \text{ K}$ , the mass heated by ionization is added directly to the outflow. To determine  $T_{\text{vir}}$ , we use the expression

$$T_{\text{vir}} = \frac{GM_{\text{vir,peak}} m_{\text{H}}}{R_{\text{vir}} k_{\text{B}}}, \quad (14)$$

$G = 6.67 \times 10^{-8} \text{ cm}^3 \text{ g}^{-1} \text{ s}^{-2}$  is the gravitational constant,  $M_{\text{vir,peak}}$  is the largest virial mass that the halo ever attains up to the current redshift, and  $k_{\text{B}} = 1.38 \times 10^{-16} \text{ cm}^2 \text{ g s}^{-2} \text{ K}^{-1}$  is the Boltzmann constant. The reasoning behind this approximation is that these haloes are not massive enough to gravitationally bind ionized gas, as the escape velocity from these haloes is smaller than the speed of sound in the ionized gas. Sufficiently strong ionizing radiation has been shown to cause efficient outflows in such haloes, quickly removing most of the gas from them (Whalen et al. 2008; Chiaki et al. 2018; Schauer et al. 2017). Visbal et al. (2017) demonstrated that haloes above the atomic cooling limit can bind ionized gas and collapse under their own gravity.

### (ii) Supernovae

Since we do not have spatial information on the gas inside a halo, we assume that a fraction of the gas absorbs the supernovae energy and is then unbound from the halo, i.e., gas is preferentially lost entirely rather than recycled via a galactic fountain. We compare the total supernovae energy deposited in the gas during time-step  $i$  with the gravitational binding energy of gas in order to determine how much gas is ejected during the time-step, i.e.,  $\delta M_{\text{out,cold}}^i$  and  $\delta M_{\text{out,hot}}^i$ . The binding energy of hot gas,  $E_{\text{bind,hot}}^i$ , is a function of the dark matter mass, disk mass (i.e., cold gas mass plus stellar mass) and hot gas itself. It can be described by the following

analytic equation,

$$E_{\text{bind,hot}}^i = \frac{3GM_{\text{vir,peak}}M_{\text{hot}}^i}{R_{\text{vir}} \left[ \frac{-R_{\text{vir}}}{R_s + R_{\text{vir}}} + \ln \frac{R_s + R_{\text{vir}}}{R_s} \right]} \times \left[ -\frac{1}{4} + \frac{1}{2} \left( 1 - \frac{R_s^2}{R_{\text{vir}}^2} \right) \ln \frac{R_s + R_{\text{vir}}}{R_s} + \frac{1}{2} \frac{R_s}{R_{\text{vir}}} \right] + \left( \frac{3R_s}{2R_{\text{vir}}} - \frac{13R_s^3}{30R_{\text{vir}}^3} \right) \frac{GM_{\text{disk}}^i M_{\text{hot}}^i}{R_s} + \frac{3}{5} \frac{G(M_{\text{hot}}^i)^2}{R_{\text{vir}}}, \quad (15)$$

where  $M_{\text{vir,peak}}$  is the virial halo mass a halo ever attains up to the current redshift,  $R_s$  is the scale radius of the dark matter halo, which we assume to follow an NFW profile (Navarro et al. 1996),  $R_{\text{vir}}$  is the virial radius of the halo and  $M_{\text{disk}}^i$  is the mass of the disk. Similarly, the binding energy of cold gas can be described by

$$E_{\text{bind,cold}}^i = \frac{3GM_{\text{vir,peak}}M_{\text{cold}}^i}{4R_s \left[ \frac{-R_{\text{vir}}}{R_s + R_{\text{vir}}} + \ln \frac{R_s + R_{\text{vir}}}{R_s} \right]} + \frac{6GM_{\text{cold}}^i M_*}{5R_s} + \frac{GM_{\text{hot}}^i M_{\text{cold}}^i}{R_{\text{vir}}} \left( \frac{3}{2} - \frac{3R_s^2}{10R_{\text{vir}}^2} \right) + \frac{3G(M_{\text{cold}}^i)^2}{5R_s}. \quad (16)$$

Complete derivations of the binding energies are presented in Appendix B2.

We adopt an outflow efficiency with a functional form of

$$\gamma_{\text{out}} = \left( \frac{M_{\text{vir,peak}}}{M_{\text{norm}}} \right)^{\alpha_{\text{out}}}, \quad (17)$$

where  $M_{\text{norm}}$  is the normalization mass. Both  $M_{\text{norm}}$  and  $\alpha_{\text{out}}$  are free parameters in our model. We adopt fiducial values of  $M_{\text{norm}} = 10^{10.5} M_{\odot}$  and  $\alpha_{\text{out}} = 0.72$  and explain their calibration in Section 3. Supernovae are assumed to explode in warm, low density regions created by prior photoionization. Therefore, we first calculate how much hot gas will be removed,

$$\delta M_{\text{out,hot}}^i = \min \left( \frac{E_{\text{SNe}}^i / \gamma_{\text{out}}}{E_{\text{bind,hot}}^i} M_{\text{hot}}^i, M_{\text{hot}}^i \right). \quad (18)$$

If  $E_{\text{SNe}} / \gamma_{\text{out}} > E_{\text{bind,hot}}^i$ , we then calculate a "leftover" supernovae energy  $E_{\text{SNe,left}}^i / \gamma_{\text{out}} = E_{\text{SNe}}^i / \gamma_{\text{out}} - E_{\text{bind,hot}}^i$ . We only consider the ejection of cold gas if  $E_{\text{SNe,left}}^i > 0$  and obtain

$$\delta M_{\text{out,cold}}^i = \min \left( \frac{E_{\text{SNe,left}}^i / \gamma_{\text{out}}}{E_{\text{bind,cold}}^i} M_{\text{cold}}^i, M_{\text{cold}}^i \right). \quad (19)$$

## 2.5 Ionizing and enriching volumes (internal/external enrichment)

Reionization feedback and external enrichment are modelled according to the description in Magg et al. (2018). Each star-forming halo has an ionized bubble around it. These bubbles are launched at the virial radius and change their sizes based on the ionizing photon budget, i.e., they expand if the halo emits more ionizing photons and shrink if there are more recombination events than ionizing photons emitted. The volume  $V$  of the ionized region is therefore updated from a time-step  $i$  to the next time-step  $i + 1$  as

$$V_{i+1} = \left( V_i + \frac{\dot{N}_{\text{ion}} \Delta t}{n} \right) (1 + \Delta t n \alpha_B C)^{-1}, \quad (20)$$

where  $\dot{N}_{\text{ion}}$  is the emission rate of ionizing photons,  $n$  is the mean IGM nucleon number density,  $C = 3$  is the clumping factor of the IGM (Robertson et al. 2013) and  $\alpha_B = 2.6 \times 10^{-13} \text{ cm}^3 \text{ s}^{-1}$  is the case B recombination rate coefficient of hydrogen at  $10^4 \text{ K}$  (Draine 2011). When haloes merge the volumes of the ionized bubbles are added up, as the sum conserves the number of ionizations.

Furthermore, each halo has a metal-enriched region around it. The expansion of the metal-enriched shell is modelled by a momentum driven snowplough, where the momentum is calculated based on the assumption that all ejected material has a constant velocity of  $v_{\text{out}} = 110 \text{ km s}^{-1}$  and slows down by sweeping up the intergalactic medium. This assumption leads to an expansion velocity of

$$v_{\text{II}} = v_{\text{out}} \frac{M_{\text{out}}}{M_{\text{out}} + \frac{4}{3} \pi \rho_b (R_{\text{enr}}^3 - R_{\text{vir}}^3)}, \quad (21)$$

where  $\rho_b$  is the mean IGM mass density and  $R_{\text{enr}}$  is the radius of the currently enriched region around the halo. Derivations and more details of the implementation of both of the methods can be found in Magg et al. (2018).

## 3 CALIBRATION AND PARAMETER STUDIES

In this section, we study the influence of the free parameters in our Pop II SF model and describe how we determine their fiducial values. These parameters are Pop II SF efficiency  $\eta_{\text{II}}$  (Eq. 7), exponent  $\alpha_{\text{out}}$ , and normalization mass  $M_{\text{norm}}$  in the outflow efficiency  $\gamma_{\text{out}}$  (Eq. 17), which are defined in Section 2. In simulations other than the fiducial one, only one parameter is varied.

### 3.1 Observables used in calibration

#### (i) MW properties at $z = 0$

We calibrate our model to the observed MW properties at  $z = 0$ , which are its stellar mass  $M_*$  (stars that survive until  $z = 0$ ) and cold gas mass  $M_{\text{cold}}$ .

#### (ii) Cumulative stellar mass function (SMF) of the satellites

The SMHM relation connects the host halo and the galaxy, but it does not provide direct information on how many satellites there are in the MW system. Therefore, we compare the cumulative stellar mass function obtained from A-SLOTH simulated satellites with the one from observed MW satellites (McConnachie 2012; Muñoz et al. 2018). To quantify the difference, we perform a two-sample Kolmogorov-Smirnov (K-S) test (Kolmogorov 1933; Smirnov 1939; Massey 1951) on our cumulative stellar mass function and the observed one. We retrieve the KS statistic from the two-sample K-S test, which represents the maximal distance between the two stellar mass functions and is normalized to have a value between 0 and 1. The smaller the KS statistic, the more-alike the two distributions are. Additionally, we retrieve a p-value from the same two-sample K-S test, which tells us whether we can reject the hypothesis that the two distributions are the same. The higher the p-value, the less certain we are to reject the hypothesis.

### (iii) Stellar mass-to-halo mass relation

We compare the SMHM relation produced by A-SLOTH with the one derived by Garrison-Kimmel et al. (2014) (hereafter GK14), who used the abundance matching (AM) to derive their SMHM relation. The underlying assumption of the AM technique is that the number of galaxies with stellar masses above a certain mass is the same as the number of haloes with virial masses above a certain mass (Kravtsov et al. 2004; Tasitsiomi et al. 2004; Vale & Ostriker 2004; Conroy et al. 2006; Conroy & Wechsler 2009; Guo et al. 2010; Behroozi et al. 2010). To quantify the difference between our SMHM relation and the one in GK14, we apply a mean-squared-error analysis. Due to observational completeness, the SMHM relation in GK14 is robust in the range  $M_* = 10^5 - 10^8 M_\odot$ . For A-SLOTH simulated galaxies with stellar masses in this range, we calculate their expected stellar mass if they follow the SMHM relation in GK14,  $AM(M_{\text{vir,peak}})$ . The mean-squared-error  $\chi^2$  is then

$$\chi^2 = \frac{1}{N_{\text{gal}}} \sum_{i=1}^{N_{\text{gal}}} (M_{*,i} - AM(M_{\text{vir},i}))^2, \quad (22)$$

where

$$\log_{10}(AM(M_*)) = (\log_{10}(5.457 \times 10^{10} M_*) + f_{\text{bwc}}(\log_{10}(M_*/3.266 \times 10^{11} M_*)) - f_{\text{bwc}}(0)), \quad (23)$$

and  $M_{\text{vir},i}$  and  $M_{*,i}$  are given in solar masses. The fitting function  $f_{\text{bwc}}$  is given in Behroozi et al. (2013) that

$$f_{\text{bwc}}(x) = -\log_{10}(10^{\alpha x} + 1) + 3.508(\log_{10}(1 + \exp(x)))^{0.316/(1 + \exp(10^{-x}))}. \quad (24)$$

We adopt  $\alpha = 1.92$  following GK14. We further compare the SMHM relation produced by A-SLOTH with the one in Nadler et al. (2020) (hereafter N20), which was inferred from the fit of satellite population discovered by the Dark Energy Survey (DES) and the Panoramic Survey Telescope and Rapid Response System Pan-STARRS1 (PS1).

## 3.2 Free parameters in the Pop II star formation model

Here we explore how A-SLOTH produced observables depend on the free parameters of our Pop II SF model. These observables are the MW properties (Figure 2), the SMHM relation, halo occupation fraction (fraction of haloes at given  $M_{\text{vir,peak}}$  that hosts a galaxy at  $z = 0$ ), and cumulative SMF of the satellites at  $z = 0$  (Figure 3). The quantification of differences in the observables are shown in Figure 4.

### (i) Pop II star formation efficiency

We explore Pop II SF efficiency  $\eta_{\text{II}}$  with 5 discrete values: [0.1, 0.5, 2.0, 5.0, 10.0]. In Figure 2, we observe that the MW stellar mass is similar among the five simulations. On the other hand, the MW cold gas mass has a clear dependence on  $\eta_{\text{II}}$ , where the highest  $\eta_{\text{II}}$  gives the lowest MW cold gas mass. In Figure 3, we observe that the SMHM relations with different  $\eta_{\text{II}}$  are all consistent with the one in GK14 and the one in N20 above the observational completeness. Below the observational completeness, haloes with similar  $M_{\text{vir,peak}}$  host smaller galaxies at  $z = 0$  if we adopt lower  $\eta_{\text{II}}$ . Similarly, the difference in the cumulative

Parameter	Fiducial value
$\eta_{\text{II}}$	2
$n_{\text{bins,II}}$	4096
$M_{\text{bound,II}} (M_\odot)$	(0.01, 100)
$M_{\text{crit}}$	S21
$\alpha_{\text{out}}$	0.72
$M_{\text{norm}} (M_\odot)$	$10^{10.5}$
$n_{\text{cold}}^{\text{den}} (\text{cm}^{-3})$	1000
$v_{\text{BC}} (\sigma_{\text{rms}})$	0.8

**Table 2.** The main parameters in our model and their fiducial values.

SMF at  $z = 0$  among the five simulations only appears below the observational completeness, where the lowest  $\eta_{\text{II}}$  gives the fewest satellites. In Figure 4, we observe that  $\eta_{\text{II}}$  has a relative small influence on the p-value and  $\chi^2$ . This indicates that the SF in satellites is mostly feedback regulated, because they have a shallow potential. The satellites grow slower than the MW throughout the merger histories, therefore, they are less resistant to the stellar feedback. On the other hand, the MW has a much deeper potential and is more capable of retaining gas.

### (ii) Outflow efficiency

As described in Section 2(ii), the amount of gas removed by SNe is determined by comparing the binding energy of gas and the energy of SNe. We introduce  $\gamma_{\text{out}} = (M_{\text{vir,peak}}/M_{\text{norm}})^{\alpha_{\text{out}}}$  such that given the same amount of SN energy, A-SLOTH removes relatively more gas in smaller haloes than in the bigger ones. Here we examine the importance of the normalization mass  $M_{\text{norm}}$  and the exponent  $\alpha_{\text{out}}$ .

We study 5 different values of  $M_{\text{norm}}$  spaced regularly in log-space between  $10^{9.5} M_\odot$  and  $10^{11.5} M_\odot$ . In contrary to  $\eta_{\text{II}}$ , we observe that changing  $M_{\text{norm}}$  leads to a change in the slope of the SMHM above the observational completeness. The slope steepens when  $M_{\text{norm}}$  decreases, but the stellar mass in the plateau is similar among the five simulations. We also find that adopting  $M_{\text{norm}} = 10^{9.5} M_\odot$  produces the most luminous satellite while adopting  $M_{\text{norm}} = 10^{11.5} M_\odot$  produces the least. There is a monotonic decrease in  $\bar{M}_*$  and  $\bar{M}_{\text{cold}}$  as  $M_{\text{norm}}$  increases. This is expected because higher  $M_{\text{norm}}$  gives lower outflow efficiency at fixed  $M_{\text{vir,peak}}$  and  $\alpha_{\text{out}}$ , which means that the halo is less resistant to the SNe. For the exponent  $\alpha_{\text{out}}$ , we study 5 different values distributed regularly in linear space between 0.40 and 1.04. We find that  $\alpha_{\text{out}}$  has an impact on the overall slope of the SMHM relation and lower  $\alpha_{\text{out}}$  gives a flatter SMHM relation. When  $\alpha_{\text{out}} > 0$ , the gas is more resistant to the SNe in haloes more massive than  $M_{\text{norm}}$ . Thus, we observe a monotonous increase in  $\bar{M}_*$  and  $\bar{M}_{\text{cold}}$  as  $\alpha_{\text{out}}$  increases.

The slope of the SMHM relation above the observational completeness is mainly influenced by  $\alpha_{\text{out}}$  and  $M_{\text{norm}}$  plays the role of the anchor point. On the other hand, the stellar mass in the SMHM plateau is mainly influenced by the Pop II star formation efficiency  $\eta_{\text{II}}$ . This leads to flattening of the SMHM relation occurring at different  $M_{\text{vir,peak}}$ .

Based on Figures 2-4, we find that the following combination of parameters gives the best overall results:  $\eta_{\text{II}} = 2.$ ,  $\alpha_{\text{out}} = 0.72$ , and  $M_{\text{norm}} = 10^{10.5} M_\odot$ . The fiducial values of our Pop II SF model are listed in Table 2.

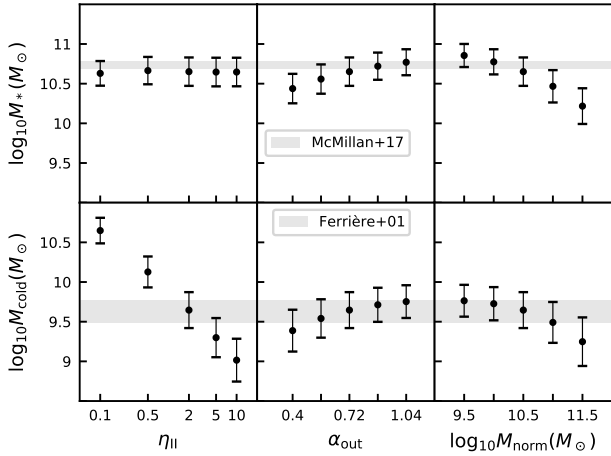


**Figure 2.** We show the mean values and standard deviations of  $M_*$  (top panels) and  $M_{\text{cold}}$  (bottom panels) from 30 *Caterpillar* trees in different simulations, where we tune one of the main parameters in the Pop II SF model. From left to right: Pop II star formation efficiency, exponent, and normalization mass in the outflow efficiency.

## 4 RESULTS

In this section we discuss about the MW properties, cumulative stellar mass function, halo occupation fraction, and SMHM relation from our fiducial model in more details and the scatter among the 30 *Caterpillar* trees.

### (i) MW properties at $z = 0$

From our fiducial model, we obtain  $\overline{M_{\text{cold}}} = 5 \times 10^9 M_{\odot}$ , and  $\overline{M_*} = 4.84 \times 10^{10} M_{\odot}$ . The corresponding standard deviations are  $\sigma_{M_{\text{cold}}} = 2.29 \times 10^9 M_{\odot}$ , and  $\sigma_{M_*} = 1.77 \times 10^{10} M_{\odot}$ , respectively. Our  $\overline{M_*}$  is at the lower limit of the estimate by [McMillan \(2017\)](#) ( $5.43 \pm 0.57 \times 10^{10} M_{\odot}$ ). The scatter in  $M_*$  among the 30 *Caterpillar* trees,  $1.77 \times 10^{10} M_{\odot}$ , is larger than the observational uncertainty,  $0.57 \times 10^{10} M_{\odot}$ . Since there is no distinction between atomic and molecular phase in our model, we compare our  $\overline{M_{\text{cold}}}$  with the combination of molecular and cold atomic masses estimated by [Ferrière \(2001\)](#). They estimated a value in the range  $3.1 - 6.0 \times 10^9 M_{\odot}$ , which covers our result of  $\overline{M_{\text{cold}}} = 5 \times 10^9 M_{\odot}$ .

### (ii) Cumulative satellite stellar mass function

In Figure 5, we show the cumulative stellar mass function (SMF) of MW satellite galaxies from our fiducial model in grey and the observed one ([McConnachie 2012](#); [Muñoz et al. 2018](#)) in blue. The scatter among the 30 *Caterpillar* trees is larger at high mass end but decreases as  $M_*$  decreases. The number of satellites increases rapidly when stellar mass goes below the observational completeness but converges at  $\approx 10^3 - 10^4 M_{\odot}$ . The discrepancy between the number of satellites below the observation limit is known to exist between observations and  $\Lambda$  cold dark matter numerical simulations, the “missing satellite problem” ([Kauffmann et al. 1993](#); [Moore et al. 1999](#); [Klypin et al. 1999](#)).

### (iii) Halo occupation fraction

In the middle panel of Figure 5 we plot individual halo occupation fractions (fraction of haloes at given  $M_{\text{vir,peak}}$  that hosts a galaxy at  $z = 0$ ) from 30 *Caterpillar* trees and find only a small scatter among them. This fraction plummets at  $M_{\text{vir,peak}} \approx 10^8 - 10^{8.5} M_{\odot}$  and stays constant while the presence and value of the stellar mass plateau changes. Thus, the presence of a plateau due to stochastically populated haloes suggested by [Sawala et al. \(2015\)](#) is not the only reason for such a break.

### (iv) Stellar mass-to-halo mass relation

In Figure 5, A-SLOTH simulated galaxies are plotted with coloured points, where the colour indicates the data density in a 2-dimensional phase space. The cyan triangles are the MWs in the 30 *Caterpillar* trees. Our fiducial model gives excellent consistency with the SMHM relation in GK14 and the one in N20. An interesting result of our model is that we predict a flattening in the SMHM relation below  $M_{\text{vir,peak}} \approx 10^9 M_{\odot}$ . Two main factors are responsible for this plateau. 1) The outflow efficiency  $\gamma_{\text{out}}$ , which is proportional to the peak virial mass of a halo (Eq. 17). In our model, one SN event ejects more gas in smaller haloes than in larger ones. In other words, gas is more easily retained in larger haloes, leading to more star formation. 2) The star formation efficiency. In Figure 3, we observe that the turn occurs at different  $M_{\text{vir,peak}}$  for different  $\eta_{\text{II}}$  and the mass of the plateau increases when  $\eta_{\text{II}}$  increases. This is because the higher the star formation efficiency, the more stars form before the SNe feedback kicks in and regulate further star formation. We fit the SMHM relation from our fiducial model with a broken power-law

$$M_* \propto M_{\text{vir,peak}}^{1.80} \quad \text{for } M_{\text{vir,peak}} \geq 10^9 M_{\odot}, \quad (25)$$

and

$$M_* \propto M_{\text{vir,peak}}^{0.66} \quad \text{for } M_{\text{vir,peak}} < 10^9 M_{\odot}. \quad (26)$$

### 4.1 Slope of the Pop II initial mass function

Here we discuss how different Pop II initial mass functions (IMFs) change our main results. To simplify the problem, we only change the slope of the Pop II IMF  $\alpha_{\text{II}}$  in the mass range  $M_{\text{star}} \geq 0.5 M_{\odot}$ . Other than the fiducial value from the Kroupa IMF,  $dN/d\log M \propto M^{-1.3}$ , we examine two different slopes, which are  $dN/d\log M \propto M^{-0.3}$  and  $dN/d\log M \propto M^{-2.3}$ , corresponding to a more top-heavy and bottom-heavy IMF, respectively. The resulting changes in the cumulative SMF, halo occupation fraction, and SMHM relation are shown in Figure 6. Green, orange, and blue represent  $\alpha_{\text{II}} = -0.3, -1.3$  and  $-2.3$ , respectively.

We find that flattening the Pop II IMF at  $M_{\text{star}} \geq 0.5 M_{\odot}$  leads to lower stellar mass at  $z = 0$  in all haloes. The cumulative SMF is therefore below the observed one at all  $M_*$ . In contrary, steepening the Pop II IMF at  $M_{\text{star}} \geq 0.5 M_{\odot}$  leads to a flattening of cumulative SMF at higher  $M_*$  and the SMF is entirely above the observed one. We find a universal turning point at  $M_{\text{vir,peak}} \approx 10^9 M_{\odot}$  and that flattening the Pop II IMF at  $M_{\text{star}} \geq 0.5 M_{\odot}$  leads to a flatter SMHM relation at  $M_{\text{vir,peak}} < 10^9 M_{\odot}$ , but does not change the slope of SMHM relation at  $M_{\text{vir,peak}} \geq 10^9 M_{\odot}$  significantly.



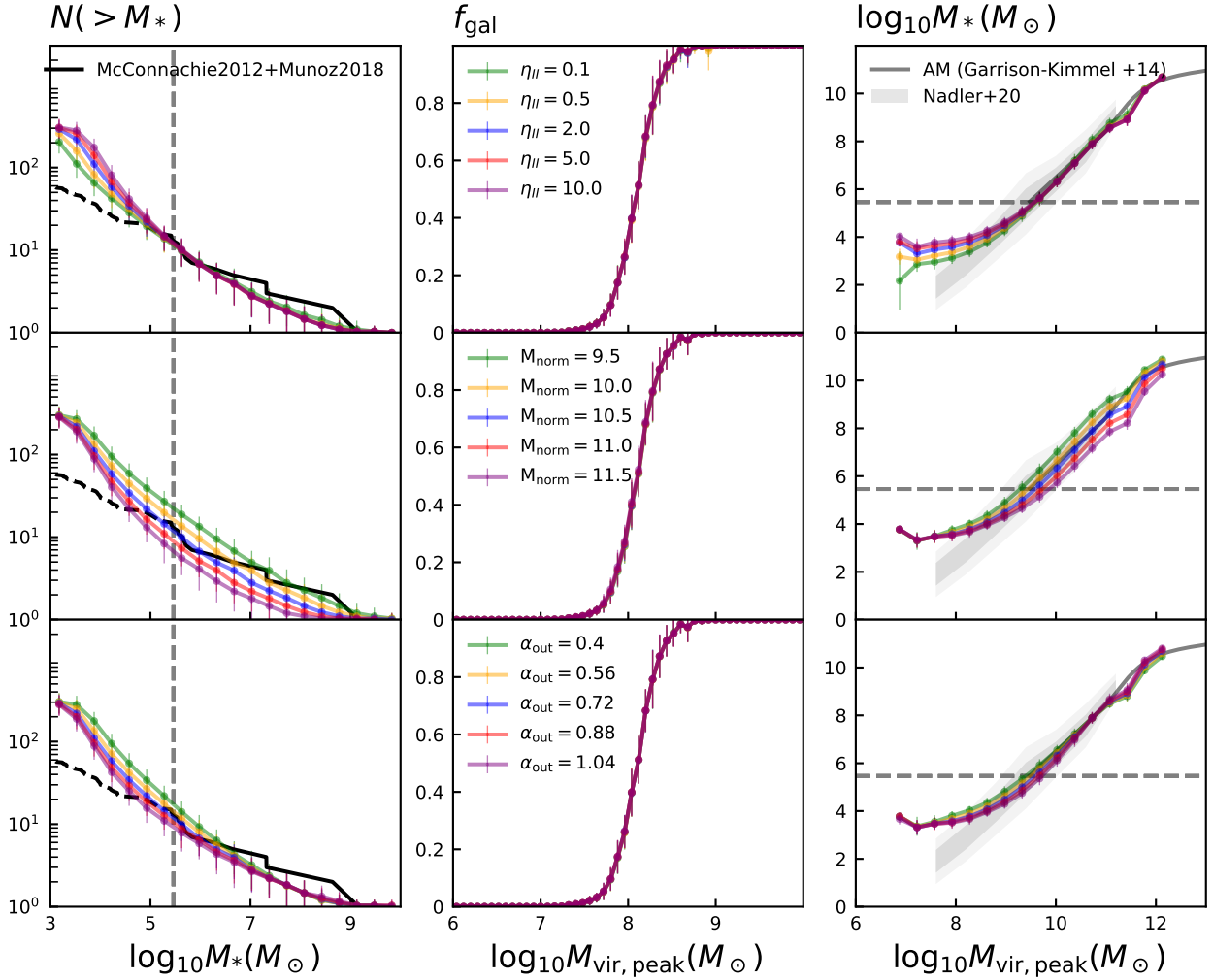


**Figure 3.** From left to right: cumulative SMF of satellites at  $z = 0$ , halo occupation fraction (fraction of haloes at a given  $M_{\text{vir,peak}}$  that hosts a galaxy at  $z = 0$ ), and the SMHM relation at  $z = 0$ . From top to bottom: Pop II star formation efficiency, normalization mass, and exponent in the outflow efficiency. In the cumulative SMF panels, we plot the observed one (McConnachie 2012; Muñoz et al. 2018) in black curve. The solid curve shows the cumulative SMF above the observational completeness, while the dashed curve shows the one below the observational completeness. In the SMHM panels, we plot the SMHM relation in GM14 in grey solid curve and the SMHM relation in N20 in grey contour. The dark grey shows  $1\sigma$  region and the light grey contour shows the  $2\sigma$  region of their best-fit relation.

Changing the Pop II IMF at the high mass end is equivalent to changing the fraction of massive stars at a fixed total stellar mass. Smaller haloes ( $M_{\text{vir,peak}} < 10^9 M_{\odot}$ ) are less resistant to the stellar feedback, therefore, not only the slope of the SMHM depends more heavily on the slope of the Pop II IMF, but also the overall distribution of stellar masses of these haloes at  $z = 0$  depends on the slope of the Pop II IMF, leading to different cumulative SMFs. The influence of different Pop II IMFs on the halo occupation fraction is negligible.

Since we only vary the slope of the Pop II IMF in these simulations, there is the possibility that we can tune the free parameters in our model to find another “good” model, which produces consistent results with the observation. However, it is not the main focus of this work to study how different Pop II IMFs influence the results. We therefore leave this exploration for future studies.

## 4.2 LW background and baryonic streaming velocity

As described in Section 2.2, the strength of the LW background ( $J_{21}$ ) and baryonic streaming velocities ( $v_{\text{BC}}$ , in units of root-mean-squared value  $\sigma_{\text{rms}}$ ) affect the critical mass  $M_{\text{crit}}$  of a halo. Here we compare different  $M_{\text{crit}}$  models with the fiducial one and examine the influence of  $v_{\text{BC}}$ .

### (i) S21

This is our fiducial model where we follow Eqs. 9 and 10 in Schauer et al. (2021) (see Section 2.2 for details). The critical mass of a halo is

$$\log_{10}M_{\text{crit}} = 6.0174(1.0 + 0.166\sqrt{J_{21}}) + 0.4159\frac{v_{\text{BC}}}{\sigma_{\text{rms}}}, \quad (27)$$

where  $J_{21}$  depends on redshift via  $J_{21} = 10^{2-z/5}$ . We note that we adopt constant  $v_{\text{BC}}$  throughout the simulation.

### (ii) OHS

In our previous work, we compute  $M_{\text{crit}}$  by considering prescriptions in O’Shea & Norman (2008), Hummel et al.

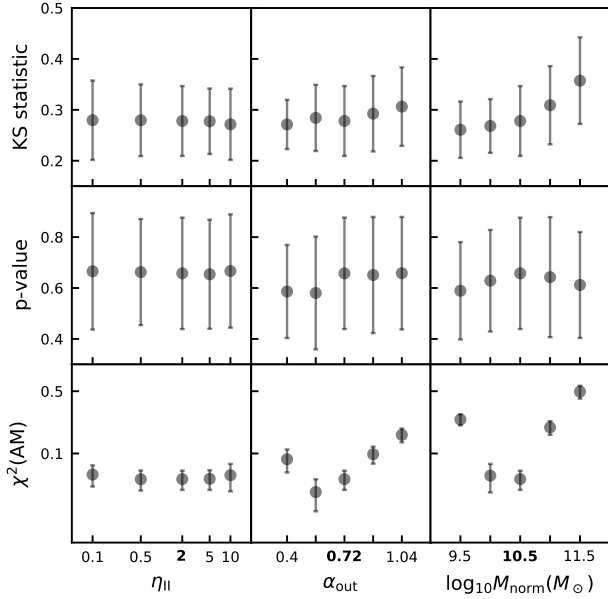


**Figure 4.** Dependence of results on the main parameters. From left to right: the Pop II SF efficiency  $\eta_{\text{II}}$ , the exponent  $\alpha_{\text{out}}$  and the normalization mass  $M_{\text{norm}}$  in the outflow efficiency. We calibrate our model with the observed MW properties, the SMHM relation (mean-squared-error  $\chi^2$ ), and the observed cumulative SMF (p-value and KS statistic). The mean values  $\pm 1\sigma$  (standard deviation among 30 *Caterpillar* trees) are shown and the fiducial value is highlighted with bold font.

(2012), and Stacy et al. (2011). Thus, we denote this model as OHS. First, we follow O’Shea & Norman (2008) and assume that  $M_{\text{crit}}$  depends only on  $J_{21}$ . We denote this critical mass as  $M_{\text{crit,O}}$  that

$$M_{\text{crit,O}} = 4 \left( 1.25 \times 10^5 + 8.7 \times 10^5 (4\pi J_{21})^{0.47} \right). \quad (28)$$

Second, we follow Hummel et al. (2012) and assume that when a halo reaches the critical virial temperature,  $T_{\text{crit}} = 2200$  K, the gas reaches high density and collapses to form Pop III stars. We denote this critical mass as  $M_{\text{crit,H}}$  and compute its value

$$M_{\text{crit,H}} = 10^6 \left( \frac{T_{\text{crit}}}{1000\text{K}} \right)^{1.5} \left( \frac{1+z}{10} \right)^{-1.5}. \quad (29)$$

Finally, we follow Stacy et al. (2011) and assume that the gas in a halo collapses and starts to form stars when the virial mass of the halo reaches a critical value. We denote this mass as  $M_{\text{crit,S}}$  and

$$M_{\text{crit,S}} = \frac{\pi v_{\text{eff}}^3}{6G^{3/2} \rho^{1/2}}, \quad (30)$$

where  $v_{\text{eff}} = \sqrt{v_{\text{BC}}(z)^2 + c_s^2}$  is the effective velocity of the gas, the redshift-dependent streaming velocity is given by

$$v_{\text{BC}}(z) = v_{\text{BC}} \times \frac{6 \times 10^5}{201} \times (1+z), \quad (31)$$

where  $v_{\text{BC}}$  is the input streaming velocity at  $z = 0$ ,  $c_s = \sqrt{k_{\text{B}}T/\mu m_{\text{H}}}$  is the sound speed,  $\rho$  is the mean dark matter density of the halo and  $T = 0.017(1+z)^2$  K is the gas

temperature (Schneider 2015). In model OHS, the final critical mass is determined by taking the maximum of  $M_{\text{crit,O}}$ ,  $M_{\text{crit,H}}$ , and  $M_{\text{crit,S}}$  that

$$M_{\text{crit}} = \text{MAX}(M_{\text{crit,O}}, M_{\text{crit,H}}, M_{\text{crit,S}}). \quad (32)$$

(iii) **F13**

The last  $M_{\text{crit}}$  model we consider is based on the prescription in Fialkov et al. (2013). In this model F13, the virial mass of a halo needs to exceed  $M_{\text{crit}}$  such that the gas cools down efficiently and starts to form stars. This critical mass is computed by

$$M_{\text{crit}} = M_0(1 + 6.96(4\pi J_{21})^{0.47}), \quad (33)$$

where  $J_{21}$  depends on redshift via  $J_{21} = 10^{2-z/5}$ , and  $M_0$  is the critical mass when there is no LW background.

In Fialkov et al. (2012), they assumed that a halo starts to form Pop III stars if its circular velocity exceeds the threshold,

$$v_{\text{cool}}(z) = \sqrt{(3.714)^2 + (4.015v_{\text{BC}}(z))^2}, \quad (34)$$

where the streaming velocity ( $z$ ) is dependent on redshift  $v_{\text{BC}}(z) = 0.0298(1+z)v_{\text{BC}}$  and  $v_{\text{BC}}$  is the initial streaming velocity. We take

$$M_0 = \left( \frac{v_{\text{cool}}(z)}{146.6\text{km/s}} \right)^3 \times \Omega_{\text{m},0}^{-0.5} \times (1+z)^{-1.5} \times 10^{12}\text{h}^{-1}, \quad (35)$$

where  $\Omega_{\text{m},0} = 0.3086$  is the matter density at  $z = 0$ . The full derivation of  $M_0$  is in Appendix D.

Finally, as described in Section 2.2, we take the minimum of  $M_{\text{crit},i}$  and  $M_{\text{crit},10^4\text{K}}$  to be the final critical mass  $M_{\text{crit,fin}}$  in model  $i$ . In total we have 3 different  $M_{\text{crit}}$  approaches: S21, OHS, and F13. We compare the results between them while varying the initial value of streaming velocity,  $v_{\text{BC}} = [0, 0.8, 2, 3]\sigma_{\text{rms}}$ . Other parameters are fixed at the fiducial values ( $\eta_{\text{II}} = 2, \alpha_{\text{out}} = 0.72, M_{\text{norm}} = 10^{10.5}M_{\odot}$ ). Kulkarni et al. (2021) also propose a new fitting formula for the critical mass. Due to the recency of their results, we were not able to include their proposed critical mass in our comparison.

We perform the same analysis as in Section 3. Despite the difference in the  $M_{\text{crit}}$  models, the influence of LW background and streaming velocity is negligible on the mean MW stellar mass as well as the satellite-based  $\chi^2$  and p-values. This indicates that we cannot tell the three  $M_{\text{crit}}$  models apart with the observables used in Section 3. We show the cumulative SMF, halo occupation fraction, and SMHM relation in Figure 7. The largest impact of LW background and streaming velocity is on smaller haloes, which is shown by the cumulative SMF and the halo occupation fraction. Model OHS produces a factor of few more ultra-faint dwarf galaxies than the other two models, regardless of the value of  $v_{\text{BC}}$ . In model S21 we find that the number of ultra-faint dwarf galaxies  $N_{\text{UFD}}$  decreases as  $v_{\text{BC}}$  increases but saturates at  $v_{\text{BC}} = 2\sigma_{\text{rms}}$ . There is a similar dependence of  $N_{\text{UFD}}$  on  $v_{\text{BC}}$  in model F13 and it produces the fewest ultra-faint dwarf galaxies among the four models when  $v_{\text{BC}} = 0$ . In Figure 8, we show  $M_{\text{crit}}$  v.s.  $z$  for different  $M_{\text{crit}}$  models with different values of  $v_{\text{BC}}$ . In our fiducial model ( $v_{\text{BC}} = 0.8\sigma_{\text{rms}}$ , F13 gives the highest  $M_{\text{crit}}$  at  $z = 10 - 15$ , followed S21, and finally OHS. This is consistent with the difference we find in  $N_{\text{UFD}}$ . The fraction of haloes hosting a galaxy decreases slower as  $M_{\text{vir,peak}}$  decreases in model OHS, whereas

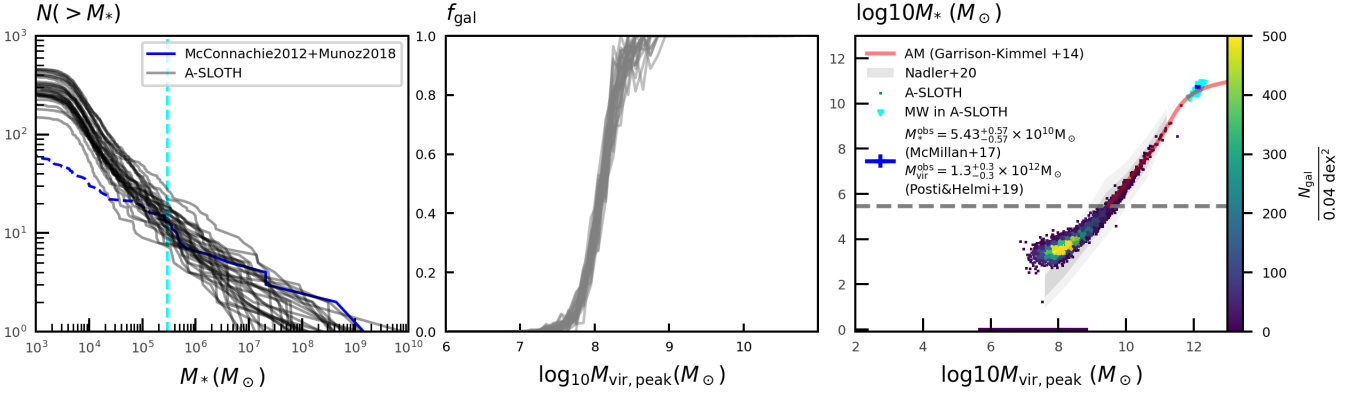


**Figure 5.** In the left panel, A-SLOTH simulated SMFs from 30 *Caterpillar* trees are shown in grey solid curves and the observed SMF (McConnachie 2012; Muñoz et al. 2018) is plotted in blue, where the dashed curve indicates that the stellar mass is below the observational completeness (shown in the cyan dashed line). In the middle panel, the halo occupation fractions from A-SLOTH simulated galaxies are shown as grey solid curves. In the right panel, each data point represents one A-SLOTH simulated galaxy and its colour indicates the data density in the parameter space. The red solid curve represents the AM relation from GK14, which is robust at  $M_* > 2.9 \times 10^5 M_\odot$ . The grey contour shows the SMHM relation from N20, where 1  $\sigma$  contour is shown in dark grey and the 2  $\sigma$  contour is shown in light grey. The grey dashed line indicates the observational completeness and below this  $M_*$ , we enter the prediction region of our model. We identify the simulated MWs with cyan triangles and the blue cross marks the observed values of MW with upper and lower limits. The MW stellar mass is estimated by McMillan (2017) and the MW virial halo mass is estimated by Posti & Helmi (2019). We show satellites with zero surviving stars at the bottom of the figure.

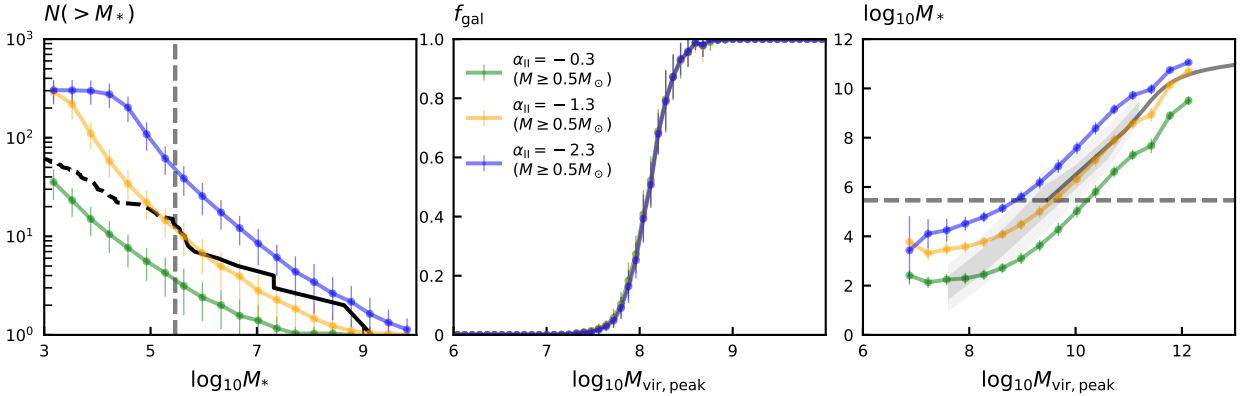


**Figure 6.** Similar to Figure 3, but we show the cumulative SMF, halo occupation fraction, and SMHM relation from different simulations where we adopt different slopes of Pop II IMF at the high mass end ( $M_{\text{star}} > 0.5 M_\odot$ ).

in models S21 and F13, this fraction experiences a plummet at  $M_{\text{vir,peak}} \approx 10^8 M_\odot$ .

## 5 DISCUSSION

### 5.1 A low-mass plateau in the stellar mass-to-halo mass relation.

The right column of Figure 3 shows our prediction that the SMHM does not continue as a single power-law to low masses, but instead reaches a plateau of roughly constant stellar mass. In A-SLOTH, this plateau is primarily due to a minimum mass scale imposed by supernova feedback: low-mass haloes able to self-quench once they form a certain amount of stars. Figure 9 shows this in detail: we run simu-

lations with different Pop II star formation efficiencies using only 1 *Caterpillar* tree. We compute the stellar mass formed before SNe occur in each global time-step ( $\Delta t_z$ )  $M_{*,\text{pre SNe}}$  and the cumulative survival stellar mass  $M_*( > z)$  for all haloes at various redshifts. At given survival stellar mass, we plot the mean  $M_{*,\text{pre SNe}}$  with 1  $\sigma$  among the haloes. We observe that with higher Pop II star formation efficiency, haloes are able to form more stars before SNe occur, which is expected. Once massive stars start to die as SNe,  $M_{*,\text{pre SNe}}$  quickly drops. Thus, if star formation is more efficient, more stars will form before SN feedback halts star formation. We emphasize that this plateau is *not* set by reionization in A-SLOTH. In this way, it may support the supernova quenching scenario proposed by earlier theoretical studies and cosmological simulations that the external ionizing background is not the dominant source to halt star formation in mini-

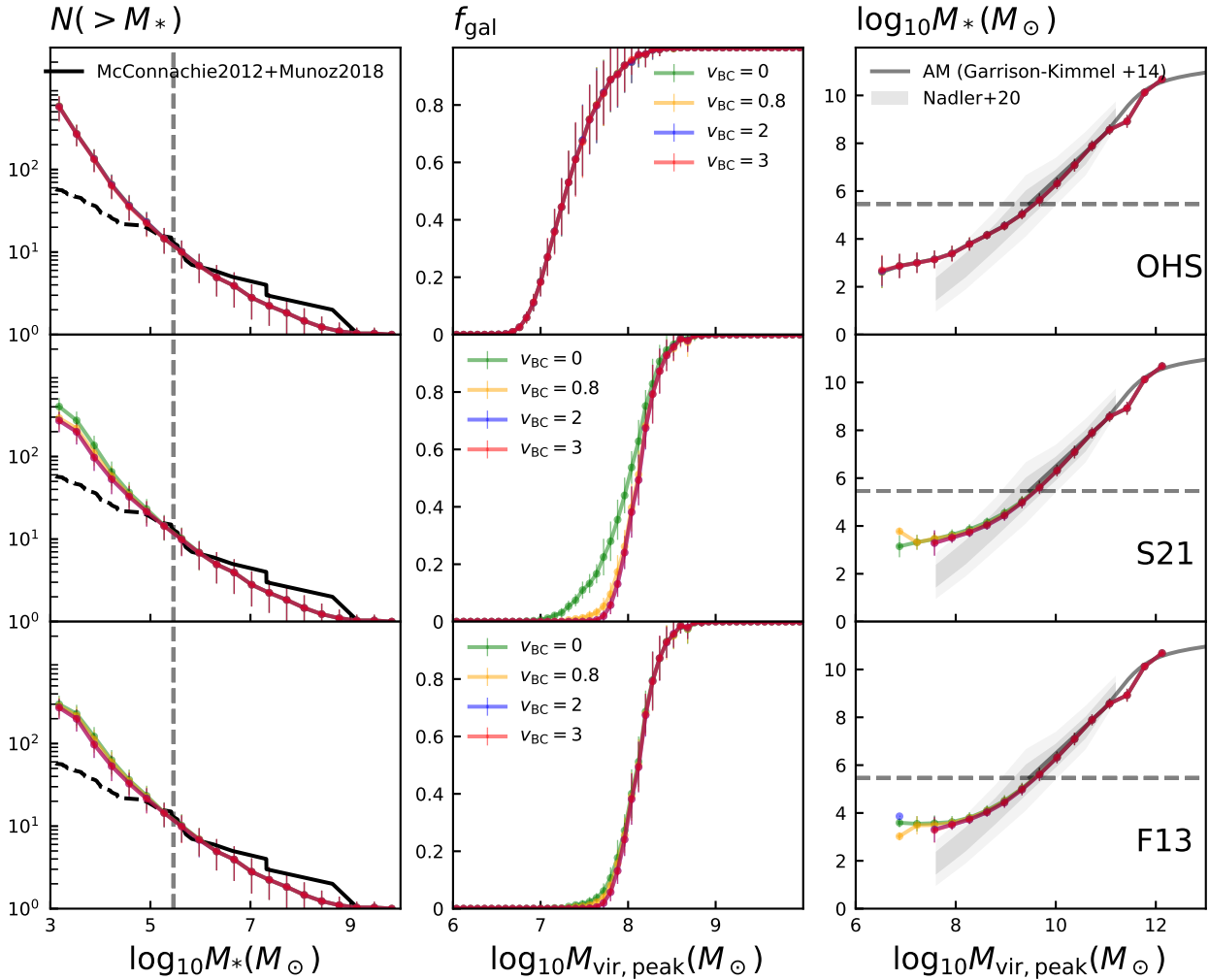


**Figure 7.** Similar to Figure 3. Here we show the cumulative SMF, halo occupation fraction, and SMHM relation from simulations where we adopt different  $M_{crit}$  models and different  $v_{BC}$ . From top to bottom: OHS, S21, and F13.

haloes (Ricotti & Gnedin 2005; Salvadori & Ferrara 2009; Bland-Hawthorn et al. 2015; Jeon et al. 2015, 2017). Recent observational studies also stress the importance of SN feedback based on the star formation histories of dwarf galaxies (Monelli et al. 2010a,b; Hidalgo et al. 2011, 2013; Gallart et al. 2021).

A similar flattening in the SMHM relation has been observed in several previous studies, but primarily driven by reionization. Sawala et al. (2015) found such a flattening of the SMHM relation in hydrodynamic simulations, though at much higher stellar masses ( $\approx 10^5 M_\odot$ ). In their simulations, this effect was primarily driven by a low occupation fraction of galaxies in haloes, due to strong global reionization at  $z = 11$ , as well as tidal stripping. This motivated Dooley et al. (2017) and Jethwa et al. (2018) to consider a “bent” SMHM relation, which is not required to explain the MW satellite luminosity function but may alleviate tensions with the SMHM relation around the LMC (also see Manwadkar & Kravtsov 2021). A similar plateau is also seen at lower stellar masses ( $\approx 10^3 M_\odot$ ) by Wheeler et al. (2015, 2019), though they emphasize this plateau could be due to resolution effects as the galaxies are composed of  $\approx 10 - 100$  star

particles only. More recently, Applebaum et al. (2021) found such a flattening as well, but also occurring at the  $\approx 10$  star particle threshold. Other analytic models have also seen a low-mass plateau in the SMHM relation, e.g. Kravtsov & Manwadkar (2021) predict a break in the SMHM relation due to reionization and scatter in halo mass growth histories. These previous results predict similar breaks in the SMHM as A-SLOTH, but for a fundamentally different reason: reionization instead of supernova feedback. Note that A-SLOTH does include local reionization through small-scale inhomogeneities, but not yet large-scale instantaneous reionization quenching at a parameterized redshift like most of these previous models.

The presence of a stellar mass plateau has several important implications. First, we predict that the luminosity function of UFDs should experience a sharp upturn at  $\approx 10^4 M_\odot$ . Dooley et al. (2017) showed that such an upturn would match the luminosity function of LMC satellites, and indeed our predicted SMHM relation matches their required SMHM relation quite closely. Second, this has implications for the minimum known dark matter halo mass. If abundance matching holds, then the lowest stellar mass



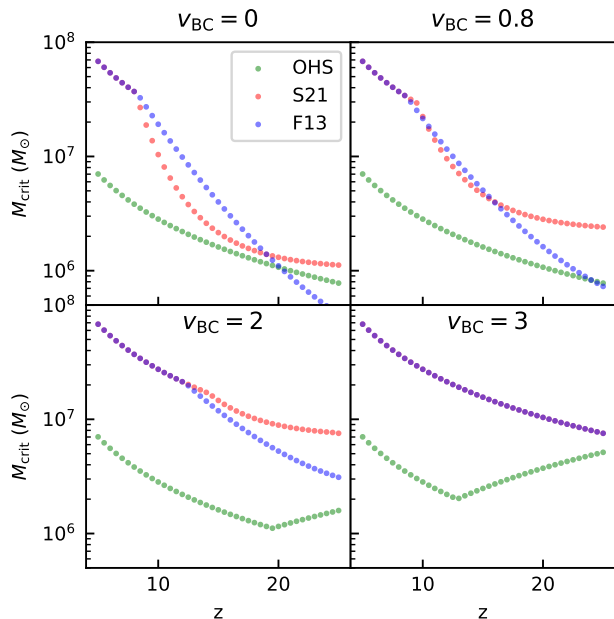


**Figure 8.**  $M_{\text{crit}}$  v.s. redshift from different  $M_{\text{crit}}$  models and different  $v_{\text{BC}}$ .

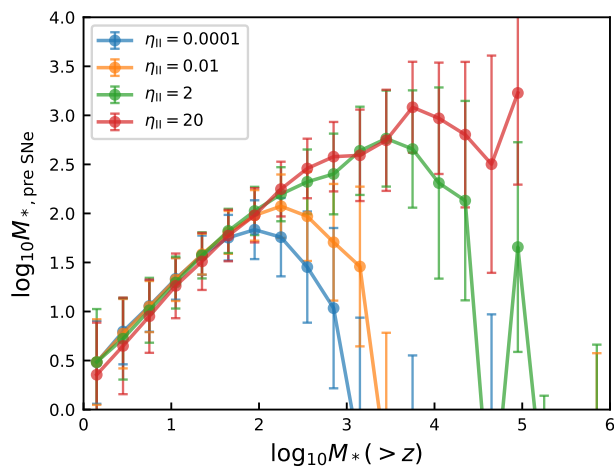


**Figure 9.**  $M_{*,\text{pre SNe}}$  v.s.  $M_*(> z)$  in haloes across all redshifts from 1 *Caterpillar* tree. Results from different simulations with different  $\eta_{\text{II}}$  are plotted with different colors along with the standard deviation. Note that  $M_{*,\text{pre SNe}}$  is computed at each redshift but  $M_*(> z)$  is cumulative over redshifts.

UFDs should reside in the lowest mass dark matter haloes, which puts constraints on the nature of dark matter (e.g., Jethwa et al. 2018; Nadler et al. 2021; Kim & Peter 2021). Such constraints often assume a single power-law can describe the SMHM relation at the low mass regime, but this would not be sufficient to describe the SMHM relation we predict here with A-SLOTH. By introducing a break in the SMHM relation, it changes the constraints obtained on dark matter properties. Finally, we note that A-SLOTH does not predict a very large scatter *around* the low-mass end of the

SMHM relation, as suggested by several previous works (e.g., Garrison-Kimmel et al. 2017; Munshi et al. 2021). This scatter is mainly due to star formation in some haloes being suppressed by reionization. When such large scatter is introduced, it actually *steepens* the intrinsic SMHM, opposite to our prediction of a minimum stellar mass scale from SN feedback.

## 5.2 Caveats

The mechanical and chemical feedback of Type Ia SNe is neglected in our current model. In the lowest-mass galaxies, Type Ia SNe can be safely ignored because they only occur with a large delay after star formation and a couple of CCSNe is enough to quench or even suppress further star formation. In the MW, Type Ia SNe (Ruiter et al. 2009) are about a factor of 5 fewer than CCSNe (Li et al. 2011; Rozwadowska et al. 2021). Thus, we do not expect the mechanical feedback from Type Ia SNe to affect our simulations substantially. We note the importance of including Type Ia SNe to correctly model the chemical abundances in the MW system, which we plan to improve in future studies.

We do not include an external ionization background in this model. The main source of ionization in our model is the emission of the MW. This choice is made for two reasons: First, if the modelled volume was cosmologically representative, we would find a Thomson scattering optical depth of  $\tau_e \approx 0.140$  from our model. We point out that we explicitly do not try to reproduce the value from the Planck observations ( $\tau_e = 0.054$  Planck Collaboration et al. 2016). The fact that our optical depth is higher than the average value inferred from Planck indicates that our modelled volume experiences earlier reionization than the Universe at large and that it is dominated by local sources. Second, except for very strong ionizing radiation fields, the LW feedback completely prevents star formation in haloes below the atomic cooling limit at redshifts below  $z \approx 14$ . Therefore reionization feedback is only a small effect in our model.

## 6 CONCLUSION

We introduce an improved Pop II SF model in the semi-analytic code A-SLOTH, which takes dark matter merger trees as input and calculates the baryonic contents in the haloes throughout its merger history. The important physical processes include Pop III and Pop II SF, as well as mechanical and chemical feedback from massive stars. The new feature in the Pop II SF model is that we are now able to trace individual Pop II stars, which allows us to precisely resolve stellar feedback in space and time. We take 30 merger trees from the *Caterpillar* project (Griffen et al. 2016) and use A-SLOTH to study the SMHM relation at  $z = 0$  of satellites in MW-like systems.

In this work, we focus on the Pop II SF model. The main free parameters are the star formation efficiency  $\eta_{\text{II}}$ , normalization mass  $M_{\text{norm}}$  and exponent  $\alpha_{\text{out}}$  in the outflow efficiency  $\gamma_{\text{out}}$ . We calibrate our model with the observed stellar mass (McMillan 2017) and cold gas mass of MW (Ferreira 2001), the SMHM relation derived with AM technique from GK14 and N20 above the observational completeness,

and the observed cumulative stellar mass function of satellite galaxies [McConnachie \(2012\)](#); [Muñoz et al. \(2018\)](#). We find  $\eta_{\text{II}} = 2$ ,  $M_{\text{norm}} = 10^{10.5} M_{\odot}$ , and  $\alpha_{\text{out}} = 0.72$  gives the most consistent results with the observation and adopt these as fiducial values.

Our fiducial model produces a mean MW stellar mass of  $4.84 \times 10^{10} M_{\odot}$  and mean cold gas mass of  $5 \times 10^9 M_{\odot}$ , which are consistent with the observed values of  $5.43 \pm 0.57 \times 10^{10} M_{\odot}$  and  $3.1 - 6.0 \times 10^9 M_{\odot}$ , respectively. The cumulative stellar mass function of MW satellite galaxies from A-SLOTH simulation is consistent with the observation above the observational completeness. We also find that the cumulative SMF has an upturn when  $M_*$  is below observational completeness and the difference between merger trees decreases. Below  $M_* \approx 10^3 - 10^4 M_{\odot}$  the cumulative SMF flattens. The fraction of haloes that host a galaxy (halo occupation fraction) increases rapidly above  $M_{\text{vir,peak}} \approx 10^8 M_{\odot}$ , and it is insensitive to the free parameters in our Pop II SF model. Our fiducial SMHM relation is consistent with the ones in GK14 and N20. We find that the slope of the SMHM relation for stellar masses is determined by the exponent  $\alpha_{\text{out}}$  and normalization mass  $M_{\text{norm}}$  in the outflow efficiency. We also observe a plateau in the SMHM relation at  $M_{\text{vir,peak}} \leq 10^9 M_{\odot}$ . This plateau represents a minimum stellar mass that forms before SNe occur and quench further star formation, which is mainly determined by the Pop II star formation efficiency  $\eta_{\text{II}}$ .

We further examine how  $\alpha_{\text{II}}$ , the slope of Pop II IMF at the high mass end ( $M_{\text{star}} > 0.5 M_{\odot}$ ), influences the results. For a top-heavy IMF, with  $\alpha_{\text{II}}$  below the [Kroupa \(2001\)](#) value, the fraction of SNe at given stellar mass is lower, leading to weaker feedback. On the contrary, for a more bottom-heavy IMF, the fraction of SNe at given stellar mass is higher and the resulting stellar feedback is stronger. Therefore, galaxies have higher stellar mass in simulations with steeper  $\alpha_{\text{II}}$  than in those with shallower  $\alpha_{\text{II}}$ . Finally, we examine the impact of different  $M_{\text{crit}}$  models and of the streaming velocity. We compare three different  $M_{\text{crit}}$  approaches: 1) the default model from Eqs. 9 and 10 in [Schauer et al. \(2021\)](#), which we denote as S21, 2) a combination of  $M_{\text{crit}}$  formulae from [O’Shea & Norman \(2008\)](#), [Hummel et al. \(2012\)](#), and [Stacy et al. \(2011\)](#), which we denote as OHS, and 3)  $M_{\text{crit}}$  formula from [Fialkov et al. \(2013\)](#), which we denote as F13. We find that model OHS produces a factor of few more ultra-faint dwarf galaxies and the effect of streaming velocity is negligible. Models S21 and F13 show similar dependence on streaming velocity that  $N_{\text{UFD}}$  decreases as  $v_{\text{BC}}$  increases and stays constant after  $v_{\text{BC}} = 2\sigma_{\text{rms}}$ . In model OHS, the halo occupation fraction experiences a slower decrease as  $M_{\text{vir,peak}}$  decreases, whereas in models S21 and F13, the halo occupation fraction experiences a plummet at  $M_{\text{vir,peak}} \approx 10^8 M_{\odot}$ .

The newly implemented Pop II SF model in A-SLOTH provides us an efficient and reliable framework to follow the formation of individual stars and their corresponding feedback at appropriate timings. This new model also enables us to examine the properties of surviving stars individually. We plan to perform follow-up studies on the properties of metal-poor stars in MW dwarf satellite galaxies at  $z = 0$ .

## ACKNOWLEDGEMENTS

We thank Yuta Tarumi for useful discussion and E. O. Nadler for providing data points to reproduce their SMHM relation. We gratefully acknowledge the data storage service SDS@hd supported by the Ministry of Science, Research and the Arts Baden-Württemberg (MWK) and the German Research Foundation (DFG) through grant INST 35/1314-1 FUGG and INST 35/1503-1 FUGG. LHC acknowledges financial support from the Deutsche Forschungsgemeinschaft (DFG) via the Collaborative Research Center (SFB 881, Project-ID 138713538) ‘The Milky Way System’ (sub-projects A1). SCOG and RSK acknowledges support from the Deutsche Forschungsgemeinschaft (DFG) via the collaborative research centre (SFB 881, Project-ID 138713538) ‘The Milky Way System’ (sub-projects A1, B1, B2 and B8) and from the Heidelberg cluster of excellence (EXC 2181 - 390900948) ‘STRUCTURES: A unifying approach to emergent phenomena in the physical world, mathematics, and complex data’. He also thanks for funding from the European Research Council in the ERC synergy grant ‘ECOGAL – Understanding our Galactic ecosystem: From the disk of the Milky Way to the formation sites of stars and planets’ (project ID 855130). TH acknowledges funding from JSPS KAKENHI Grant Numbers 19K23437 and 20K14464.

## DATA AVAILABILITY

The data underlying this article will be shared on reasonable request to the corresponding author.

## REFERENCES

- Applebaum E., Brooks A. M., Christensen C. R., Munshi F., Quinn T. R., Shen S., Tremmel M., 2021, *ApJ*, **906**, 96
- Behroozi P. S., Conroy C., Wechsler R. H., 2010, *ApJ*, **717**, 379
- Behroozi P. S., Wechsler R. H., Conroy C., 2013, *ApJ*, **770**, 57
- Bland-Hawthorn J., Sutherland R., Webster D., 2015, *ApJ*, **807**, 154
- Bryan G. L., Norman M. L., 1998, *ApJ*, **495**, 80
- Chiaki G., Susa H., Hirano S., 2018, *MNRAS*, **475**, 4378
- Conroy C., Wechsler R. H., 2009, *ApJ*, **696**, 620
- Conroy C., Wechsler R. H., Kravtsov A. V., 2006, *ApJ*, **647**, 201
- Cowie L. L., McKee C. F., Ostriker J. P., 1981, *ApJ*, **247**, 908
- Dooley G. A., Peter A. H. G., Carlin J. L., Frebel A., Bechtol K., Willman B., 2017, *MNRAS*, **472**, 1060
- Draine B. T., 2011, *Physics of the interstellar and intergalactic medium*. Princeton Univ. Press
- Drlica-Wagner A., et al., 2015, *ApJ*, **813**, 109
- Drlica-Wagner A., et al., 2020, *ApJ*, **893**, 47
- Ekström S., Meynet G., Chiappini C., Hirschi R., Maeder A., 2008, *A&A*, **489**, 685
- Engler C., et al., 2021, arXiv e-prints, [p. arXiv:2101.12215](#)
- Ferrière K. M., 2001, *Reviews of Modern Physics*, **73**, 1031
- Fialkov A., Barkana R., Tseliakhovich D., Hirata C. M., 2012, *MNRAS*, **424**, 1335
- Fialkov A., Barkana R., Visbal E., Tseliakhovich D., Hirata C. M., 2013, *MNRAS*, **432**, 2909
- Font A. S., et al., 2020, *MNRAS*, **498**, 1765
- Font A. S., McCarthy I. G., Belokurov V., 2021, *MNRAS*, **505**, 783
- Gallart C., et al., 2021, *ApJ*, **909**, 192
- Garrison-Kimmel S., Boylan-Kolchin M., Bullock J. S., Lee K., 2014, *MNRAS*, **438**, 2578

- Garrison-Kimmel S., Bullock J. S., Boylan-Kolchin M., Bardwell E., 2017, *MNRAS*, **464**, 3108
- Greif T. H., Bromm V., 2006, *MNRAS*, **373**, 128
- Griffen B. F., Ji A. P., Dooley G. A., Gómez F. A., Vogelsberger M., O’Shea B. W., Frebel A., 2016, *ApJ*, **818**, 10
- Guo Q., White S., Li C., Boylan-Kolchin M., 2010, *MNRAS*, **404**, 1111
- Hartwig T., Bromm V., Klessen R. S., Glover S. C. O., 2015, *MNRAS*, **447**, 3892
- Hartwig T., et al., 2018, *MNRAS*, **478**, 1795
- Hartwig T., Ishigaki M. N., Klessen R. S., Yoshida N., 2019, *MNRAS*, **482**, 1204
- Heger A., Woosley S. E., 2002, *ApJ*, **567**, 532
- Heger A., Woosley S. E., 2010, *ApJ*, **724**, 341
- Hidalgo S. L., et al., 2011, *ApJ*, **730**, 14
- Hidalgo S. L., et al., 2013, *ApJ*, **778**, 103
- Hopkins P. F., Kereš D., Oñorbe J., Faucher-Giguère C.-A., Quataert E., Murray N., Bullock J. S., 2014, *MNRAS*, **445**, 581
- Hummel J. A., Pawlik A. H., Milosavljević M., Bromm V., 2012, *ApJ*, **755**, 72
- Ishigaki M. N., Tominaga N., Kobayashi C., Nomoto K., 2014, *ApJ*, **792**, L32
- Ishigaki M. N., Tominaga N., Kobayashi C., Nomoto K., 2018, *ApJ*, **857**, 46
- Jeon M., Bromm V., Pawlik A. H., Milosavljević M., 2015, *MNRAS*, **452**, 1152
- Jeon M., Besla G., Bromm V., 2017, *ApJ*, **848**, 85
- Jethwa P., Erkal D., Belokurov V., 2018, *MNRAS*, **473**, 2060
- Kauffmann G., White S. D. M., Guiderdoni B., 1993, *MNRAS*, **264**, 201
- Kim S. Y., Peter A. H. G., 2021, arXiv e-prints, p. arXiv:2106.09050
- Klessen R. S., Glover S. C. O., 2016, *Saas-Fee Advanced Course*, **43**, 85
- Klypin A., Gottlöber S., Kravtsov A. V., Khokhlov A. M., 1999, *ApJ*, **516**, 530
- Kobayashi C., Tominaga N., Nomoto K., 2011, *ApJ*, **730**, L14
- Kolmogorov A. N., 1933, *Giornale dell’Istituto Italiano degli Attuari*, **4**, 83
- Koposov S. E., Belokurov V., Torrealba G., Evans N. W., 2015, *ApJ*, **805**, 130
- Kravtsov A., Manwadkar V., 2021, arXiv e-prints, p. arXiv:2106.09724
- Kravtsov A. V., Berlind A. A., Wechsler R. H., Klypin A. A., Gottlöber S., Allgood B., Primack J. R., 2004, *ApJ*, **609**, 35
- Kroupa P., 2001, *MNRAS*, **322**, 231
- Kulkarni M., Visbal E., Bryan G. L., 2021, *ApJ*, **917**, 40
- Lacey C., Cole S., 1993, *MNRAS*, **262**, 627
- Li W., Chornock R., Leaman J., Filippenko A. V., Poznanski D., Wang X., Ganeshalingam M., Mannucci F., 2011, *MNRAS*, **412**, 1473
- Libeskind N. I., et al., 2020, *MNRAS*, **498**, 2968
- Magg M., Hartwig T., Agarwal B., Frebel A., Glover S. C. O., Griffen B. F., Klessen R. S., 2018, *MNRAS*, **473**, 5308
- Manwadkar V., Kravtsov A., 2021, arXiv e-prints, p. arXiv:2112.04511
- Marigo P., Girardi L., Chiosi C., Wood P. R., 2001, *A&A*, **371**, 152
- Massey Frank J. J., 1951, *Journal of the American Statistical Association*, **46**, 68
- McConnachie A. W., 2012, *AJ*, **144**, 4
- McMillan P. J., 2017, *MNRAS*, **465**, 76
- Monelli M., et al., 2010a, *ApJ*, **720**, 1225
- Monelli M., et al., 2010b, *ApJ*, **722**, 1864
- Moore B., Ghigna S., Governato F., Lake G., Quinn T., Stadel J., Tozzi P., 1999, *ApJ*, **524**, L19
- Muñoz R. R., Côté P., Santana F. A., Geha M., Simon J. D., Oyarzún G. A., Stetson P. B., Djorgovski S. G., 2018, *ApJ*, **860**, 66
- Munshi F., Brooks A. M., Applebaum E., Christensen C. R., Quinn T., Sligh S., 2021, *ApJ*, **923**, 35
- Nadler E. O., et al., 2020, *ApJ*, **893**, 48
- Nadler E. O., Banerjee A., Adhikari S., Mao Y.-Y., Wechsler R. H., 2021, *ApJ*, **920**, L11
- Navarro J. F., Frenk C. S., White S. D. M., 1996, *ApJ*, **462**, 563
- Nomoto K., Kobayashi C., Tominaga N., 2013, *ARA&A*, **51**, 457
- O’Shea B. W., Norman M. L., 2008, *ApJ*, **673**, 14
- Planck Collaboration et al., 2014, *A&A*, **571**, A16
- Planck Collaboration et al., 2016, *A&A*, **594**, A13
- Posti L., Helmi A., 2019, *A&A*, **621**, A56
- Press W. H., Schechter P., 1974, *ApJ*, **187**, 425
- Ricotti M., Gnedin N. Y., 2005, *ApJ*, **629**, 259
- Ritter J. S., Sluder A., Safrank-Shrader C., Milosavljević M., Bromm V., 2015, *MNRAS*, **451**, 1190
- Robertson B. E., et al., 2013, *ApJ*, **768**, 71
- Rossi M., Salvadori S., Skúladóttir Á., 2021, *MNRAS*, **503**, 6026
- Rozwadowska K., Vissani F., Cappellaro E., 2021, *New Astron.*, **83**, 101498
- Ruiter A. J., Belczynski K., Fryer C., 2009, *ApJ*, **699**, 2026
- Salvadori S., Ferrara A., 2009, *MNRAS*, **395**, L6
- Salvadori S., Skúladóttir Á., Tolstoy E., 2015, *MNRAS*, **454**, 1320
- Sawala T., et al., 2015, *MNRAS*, **448**, 2941
- Schaerer D., 2002, *A&A*, **382**, 28
- Schauer A. T. P., et al., 2017, *MNRAS*, **467**, 2288
- Schauer A. T. P., Glover S. C. O., Klessen R. S., Clark P., 2021, *MNRAS*, **507**, 1775
- Schneider P., 2015, *Extragalactic Astronomy and Cosmology: An Introduction*. Springer-Verlag Berlin Heidelberg, doi:10.1007/978-3-642-54083-7
- Smirnov N. V., 1939, *Bull. Math. Univ. Moscou*, **2**, 3
- Sormani M. C., Treß R. G., Klessen R. S., Glover S. C. O., 2017, *MNRAS*, **466**, 407
- Spitzer L., 1978, *Physical processes in the interstellar medium*. New York Wiley-Interscience, doi:10.1002/9783527617722
- Stacy A., Bromm V., Loeb A., 2011, *ApJ*, **730**, L1
- Tarumi Y., Hartwig T., Magg M., 2020, *ApJ*, **897**, 58
- Tasitsiomi A., Kravtsov A. V., Wechsler R. H., Primack J. R., 2004, *ApJ*, **614**, 533
- Torrealba G., Koposov S. E., Belokurov V., Irwin M., 2016, *MNRAS*, **459**, 2370
- Torrealba G., et al., 2018, *MNRAS*, **475**, 5085
- Vale A., Ostriker J. P., 2004, *MNRAS*, **353**, 189
- Visbal E., Bryan G. L., Haiman Z., 2017, *MNRAS*, **469**, 1456
- Visbal E., Haiman Z., Bryan G. L., 2018, *MNRAS*, **475**, 5246
- Visbal E., Bryan G. L., Haiman Z., 2020, *ApJ*, **897**, 95
- Wetzel A. R., Hopkins P. F., Kim J.-h., Faucher-Giguère C.-A., Kereš D., Quataert E., 2016, *ApJ*, **827**, L23
- Whalen D., van Veelen B., O’Shea B. W., Norman M. L., 2008, *ApJ*, **682**, 49
- Wheeler C., Oñorbe J., Bullock J. S., Boylan-Kolchin M., Elbert O. D., Garrison-Kimmel S., Hopkins P. F., Kereš D., 2015, *MNRAS*, **453**, 1305
- Wheeler C., et al., 2019, *MNRAS*, **490**, 4447
- Willman B., 2010, *Advances in Astronomy*, **2010**, 285454
- de Bannassuti M., Schneider R., Valiante R., Salvadori S., 2014, *MNRAS*, **445**, 3039
- de Bannassuti M., Salvadori S., Schneider R., Valiante R., Omukai K., 2017, *MNRAS*, **465**, 926

$n_{\text{bins,II}}$	$N_{\text{ion}}$	$N_{\text{SNe}}$
128	10.69	7.85
256	10.55	7.75
512	10.48	7.71
1024	10.51	7.73
2048	10.49	7.74
4096	10.49	7.74
8192	10.48	7.74
16384	10.48	7.74

**Table A1.** Averaged number of ionizing stars and SNe that we draw from the IMF given a total stellar mass of  $1000M_{\odot}$ .

## APPENDIX A: CHOICE OF NUMBER OF POP II IMF BINS

We show the averaged number of ionizing stars and SNe we get out of every  $1000M_{\odot}$  of stars in our model in Table A1 with different number of Pop II IMF bins  $n_{\text{bins,II}}$ . The difference between 4096 and 8192 bins is less than 0.1% in  $N_{\text{ion}}$  and identical in  $N_{\text{SNe}}$ . Therefore, we adopt  $n_{\text{bins,II}} = 4096$  in our model.

## APPENDIX B: DETAILED DERIVATION OF MASS CONVERSION RATE AND GAS BINDING ENERGY

### B1 Mass conversion rate

Here we describe the derivation of Eq. 12. We first calculate the mass which is enclosed in the HII region of a D-type I-front, which can be described as a function of  $t$

$$M_{\text{HII}} = m_{\text{H}} \frac{4\pi}{3} R_{\text{i}}^3(t) n_{\text{HII}}(t) \text{ [g]}, \quad (\text{B1})$$

where  $n_{\text{HII}}(t)$  is the number density at time  $t$  inside the HII region and  $m_{\text{H}}$  is the atomic mass. For simplicity, we ignore helium. The number density inside the HII region is computed by

$$n_{\text{HII}}(t) = n_{\text{cold}}^{\text{den}} \left( \frac{R_{\text{D}}}{R_{\text{i}}(t)} \right)^{3/2}, \quad (\text{B2})$$

where  $n_{\text{cold}}^{\text{den}}$  is the number density of the dense gas. The radius that the I-front reaches at time  $t$ ,  $R_{\text{i}}(t)$  is computed by (Spitzer 1978)

$$R_{\text{i}}(t) = R_{\text{D}} \left[ 1 + \frac{7}{4} \frac{c_{\text{s}}(t - t_{\text{D}})}{R_{\text{D}}} \right]^{4/7} \text{ (cm)}, \quad (\text{B3})$$

where  $c_{\text{s}} = 11.4 \left( \frac{T_{\text{ion}}}{T_4} \right)^{1/2} \times 10^5 \text{ cm s}^{-1}$  is the sound speed and we assume for simplicity a fixed temperature  $T_{\text{ion}} = 10^4 \text{ K}$ . The distance that the I-front reaches when it enters D-type expansion,  $R_{\text{D}}$ , is

$$R_{\text{D}} = \left( \frac{3Q}{4\pi n_0^2 \alpha_{\text{B}}} \right)^{1/3} \text{ ((cm))}, \quad (\text{B4})$$

and the time it needs to reach this distance,  $t_{\text{D}}$ , is given by

$$t_{\text{D}} = \ln \left( \frac{842}{23} \left( \frac{Q}{10^{48}} \right)^{1/3} \left( \frac{n_{\text{cold}}^{\text{den}}}{10^3} \right)^{1/3} \right) \tau \text{ (s)}, \quad (\text{B5})$$

where  $\tau = (\alpha_{\text{B}} n_{\text{cold}}^{\text{den}})^{-1} \text{ s}$  is the recombination time. We compute the time derivative of  $R_{\text{i}}(t)$ ,

$$\frac{dR_{\text{i}}(t)}{dt} = c_{\text{s}} \left[ 1 + \frac{7}{4} \frac{c_{\text{s}}(t - t_{\text{D}})}{R_{\text{D}}} \right]^{-3/7}. \quad (\text{B6})$$

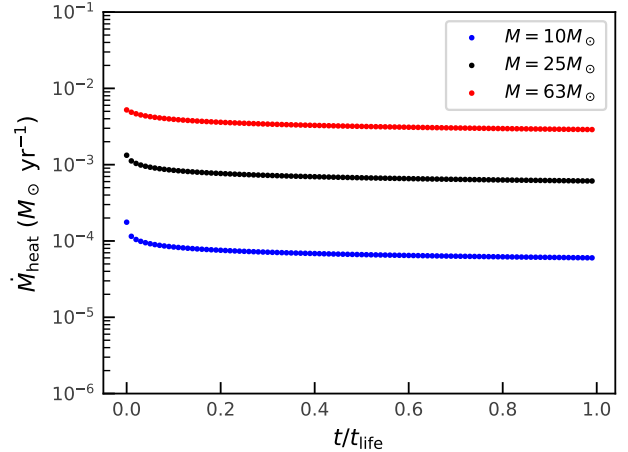


**Figure B1.** Mass conversion rate of 10, 25, and 63  $M_{\odot}$  stars throughout their lifetimes. These values are computed using Equation B8 with an assumed cold gas density of  $n_{\text{cold}}^{\text{den}} = 1000 \text{ cm}^{-3}$ .

We can then express  $M_{\text{HII}}(t)$  as

$$\begin{aligned} M_{\text{HII}}(t) &= \frac{4\pi m_{\text{H}}}{3} R_{\text{D}}^3 \left[ 1 + \frac{7}{4} \frac{c_{\text{s}}(t - t_{\text{D}})}{R_{\text{D}}} \right]^{12/7} n_{\text{cold}}^{\text{den}} \left( \frac{R_{\text{D}}}{R_{\text{i}}(t)} \right)^{3/2} \quad (\text{B7}) \\ &= m_{\text{H}} n_{\text{cold}}^{\text{den}} \frac{4\pi}{3} R_{\text{D}}^3 \left[ 1 + \frac{7}{4} \frac{c_{\text{s}}(t - t_{\text{D}})}{R_{\text{D}}} \right]^{6/7} \text{ (g)}. \end{aligned}$$

Finally, we can use the expression above to write down the rate at which gas is incorporated into the HII region, converting it from the cold phase in our model to the hot phase. This mass conversion rate is given as a function of time,  $Q$  and  $n_{\text{cold}}^{\text{den}}$  by

$$\begin{aligned} \dot{M}_{\text{heat}} &= 10^{-25} m_{\text{H}} R_{\text{D}}^2 c_{\text{s}} \left[ 1 + \frac{7}{4} \frac{c_{\text{s}}(t - t_{\text{D}})}{R_{\text{D}}} \right]^{-1/7} \\ & n_{\text{cold}}^{\text{den}} (M_{\odot} \text{ yr}^{-1}). \end{aligned} \quad (\text{B8})$$

As an example, we show the mass conversion rates for 10, 25 and  $63M_{\odot}$  stars over the course of their lives in Figure B1. These values were computed assuming a cold gas density  $n_{\text{cold}}^{\text{den}} = 1000 \text{ cm}^{-3}$ , but are only weakly sensitive to this choice.

After a decrease in a small fraction of the stellar lifetime,  $\dot{M}_{\text{heat}}$  stays almost constant until the end of the stellar lifetime. Based on Table 6 in Schaerer (2002), we find that the ionizing photon rate  $Q$  of massive stars ( $7\text{-}150M_{\odot}$ ) can be well described with the following equation,

$$\begin{aligned} \log_{10} Q &= 27.8 + 30.68 \left( \frac{M_{\text{star}}}{M_{\odot}} \right) \\ & - 14.8 \left( \frac{M_{\text{star}}}{M_{\odot}} \right)^2 + 2.59 \left( \frac{M_{\text{star}}}{M_{\odot}} \right)^3. \end{aligned} \quad (\text{B9})$$

### B2 Gas binding energy

Here we show the full derivation of cold and hot gas binding energies that are used to determine the outflow mass in



Section 2(ii). Without spatial information of the baryons, we assume a uniform density inside each baryonic content. There are four components that contribute to the total binding energy: the dark matter halo, the cold gas, the hot gas and the stars. Stars and cold gas reside in the same region, that we define as the disk (innermost 5% region in terms of radius). The contribution from each component can be calculated separately and summed up later to give Eqs. B10 and B14.

$$\begin{aligned}
E_{\text{bind,hot}} &= \int_0^{R_{\text{vir}}} dM_{\text{hot}} U(r) \\
&= E_{\text{hot,DM}} + E_{\text{hot,disk}} + E_{\text{hot,hot}} \\
&= \int_0^{R_{\text{vir}}} dM_{\text{hot}} U_{\text{DM}}(r) + \int_0^{R_{\text{vir}}} dM_{\text{hot}} U_{\text{disk}}(r) \\
&+ \int_0^{R_{\text{vir}}} dM_{\text{hot}} U_{\text{hot}}(r),
\end{aligned} \tag{B10}$$

where  $U$  is the potential energy.

$$\begin{aligned}
E_{\text{hot,hot}} &= \int_0^{R_{\text{vir}}} \frac{GM_{\text{hot}}(r)dM_{\text{hot}}}{R} \\
&= \int_0^{R_{\text{vir}}} \frac{G\frac{4}{3}\pi r^3 \rho_{\text{hot}} 4\pi r^2 \rho_{\text{hot}} dr}{r} \\
&= \frac{3}{5} \frac{GM_{\text{hot}}^2}{R_{\text{vir}}}.
\end{aligned} \tag{B11}$$

$$\begin{aligned}
E_{\text{hot,disk}} &= \int_0^{R_{\text{vir}}} dM_{\text{hot}} \int_r^\infty \frac{GM_{\text{disk}}(R)}{R^2} dR \\
&= \int_0^{R_s} dM_{\text{hot}} \left[ \int_r^{R_s} \frac{GM_{\text{disk}}(R)}{R^2} dR + \int_{R_s}^\infty \frac{GM_{\text{disk}}}{R^2} dR \right] \\
&+ \int_{R_s}^{R_{\text{vir}}} dM_{\text{hot}} \frac{GM_{\text{disk}}}{r} \\
&= 4\pi \rho_{\text{hot}} \left[ G \frac{2\pi \left( \frac{R_s^3}{3} R_s^2 - \frac{R_s^5}{5} \right) \rho_{\text{disk}}}{3} + \frac{R_s^3}{3} \frac{GM_{\text{disk}}}{R_s} \right] \\
&+ 2\pi \rho_{\text{hot}} (R_{\text{vir}}^2 - R_s^2) GM_{\text{disk}} \\
&= \left( \frac{3R_s}{2R_{\text{vir}}} - \frac{13R_s^3}{30R_{\text{vir}}^3} \right) \frac{GM_{\text{hot}} M_{\text{disk}}}{R_s},
\end{aligned} \tag{B12}$$

where  $M_{\text{disk}} = M_{\text{stellar}} + M_{\text{cold}}$ .

$$\begin{aligned}
E_{\text{hot,DM}} &= \int_0^{R_{\text{vir}}} dM_{\text{hot}} \int_r^\infty \frac{GM_{\text{DM}}(R)}{R^2} dR \\
&= \int_0^{R_{\text{vir}}} dM_{\text{hot}} \int_r^\infty \frac{G}{R^2} dR \int_0^R 4\pi r'^2 \frac{\rho_0}{\frac{r'}{R_s} \left( 1 + \frac{r'}{R_s} \right)^2} dr' \\
&= 4\pi G \rho_0 R_s^3 \int_0^{R_{\text{vir}}} dM_{\text{hot}} \int_r^\infty \frac{dR}{R^2} \int_0^R \frac{r'}{(R_s + r')^2} dr' \\
&= 16\pi^2 G \rho_0 \rho_{\text{hot}} R_s^3 \int_0^{R_{\text{vir}}} r (\ln(R_s + r) - \ln R_s) dr \\
&= \frac{3GM_{\text{vir,peak}} M_{\text{hot}}}{R_{\text{vir}} \left[ \frac{-R_{\text{vir}}}{R_s + R_{\text{vir}}} + \ln \frac{R_s + R_{\text{vir}}}{R_s} \right]} \times \\
&\left[ \frac{1}{2} \left( 1 - \frac{R_s^2}{R_{\text{vir}}^2} \right) \ln \left( \frac{R_s + R_{\text{vir}}}{R_s} \right) + \frac{1}{2} \left( \frac{R_s}{R_{\text{vir}}} \right) - \frac{1}{4} \right]
\end{aligned}$$

(B13)

Similarly, the total binding energy of cold gas can be decomposed into four components:

$$\begin{aligned}
E_{\text{bind,cold}} &= \int_0^{R_s} dM_{\text{cold}} U(r) \\
&= E_{\text{cold,DM}} + E_{\text{cold,stellar}} + E_{\text{cold,cold}} + E_{\text{cold,hot}}
\end{aligned} \tag{B14}$$

$$\begin{aligned}
E_{\text{cold,stellar}} &= \int_0^{R_s} dM_{\text{cold}} \int_r^\infty \frac{GM_*(R)}{R^2} dR \\
&= \int_0^{R_s} dM_{\text{cold}} \left[ \int_r^{R_s} \frac{GM_*(R)}{R^2} dR + \int_{R_s}^\infty \frac{GM_*(R)}{R^2} dR \right] \\
&= \int_0^{R_s} 4\pi r^2 \rho_{\text{cold}} dr \left[ \frac{G2\pi \rho_{\text{star}} (R_s^2 - r^2)}{3} + \frac{GM_*}{R_s} \right] \\
&= 4\pi \rho_{\text{cold}} \left[ \frac{G2\pi \rho_{\text{star}} \left( \frac{R_s^3}{3} R_s^2 - \frac{R_s^5}{5} \right)}{3} + \frac{GM_* R_s^3}{3R_s} \right] \\
&= \frac{6GM_{\text{cold}} M_*}{5R_s}
\end{aligned} \tag{B15}$$

$$\begin{aligned}
E_{\text{cold,hot}} &= \int_0^{R_s} dM_{\text{cold}} \int_r^\infty \frac{GM_{\text{hot}}(R)}{R^2} dR \\
&= \int_0^{R_s} dM_{\text{cold}} \left[ \int_r^{R_{\text{vir}}} \frac{GM_{\text{hot}}(R)}{R^2} dR + \int_{R_{\text{vir}}}^\infty \frac{GM_{\text{hot}}(R)}{R^2} dR \right] \\
&= \int_0^{R_s} \rho_{\text{cold}} 4\pi r^2 dr \left[ \frac{G\rho_{\text{hot}} 2\pi (R_{\text{vir}}^2 - r^2)}{3} + \frac{GM_{\text{hot}}}{R_{\text{vir}}} \right] \\
&= \rho_{\text{cold}} 4\pi \left[ \frac{G\rho_{\text{hot}} 2\pi \left( \frac{R_s^3}{3} R_{\text{vir}}^2 - \frac{R_s^5}{5} \right)}{3} + \frac{GM_{\text{hot}} R_s^3}{3R_{\text{vir}}} \right] \\
&= \frac{GM_{\text{hot}} M_{\text{cold}}}{R_{\text{vir}}} \left( \frac{3}{2} - \frac{3R_s^2}{10R_{\text{vir}}^2} \right)
\end{aligned} \tag{B16}$$

$$\begin{aligned}
E_{\text{cold,DM}} &= \int_0^{R_s} dM_{\text{cold}} \int_r^\infty \frac{GM_{\text{DM}}(R)}{R^2} dR \\
&= 16\pi^2 G \rho_0 \rho_{\text{cold}} R_s^3 \int_0^{R_s} r (\ln(R_s + r) - \ln R_s) dr \\
&= \frac{3GM_{\text{vir,peak}} M_{\text{cold}}}{4R_s \left[ \frac{-R_{\text{vir}}}{R_s + R_{\text{vir}}} + \ln \frac{R_s + R_{\text{vir}}}{R_s} \right]}
\end{aligned} \tag{B17}$$

Finally,  $E_{\text{cold,cold}}$  can be estimated by

$$E_{\text{cold,cold}} = \frac{3GM_{\text{cold}}^2}{5R_s} \tag{B18}$$

### APPENDIX C: CLUSTERED VS. INDIVIDUAL HII REGIONS

As derived in Appendix B1,  $\dot{M}_{\text{heat}}$  does not depend linearly on the number of ionizing photons. Therefore, whether stars are in clusters or isolation is important to the stellar feedback. We show two extreme cases of star clustering: 1) all

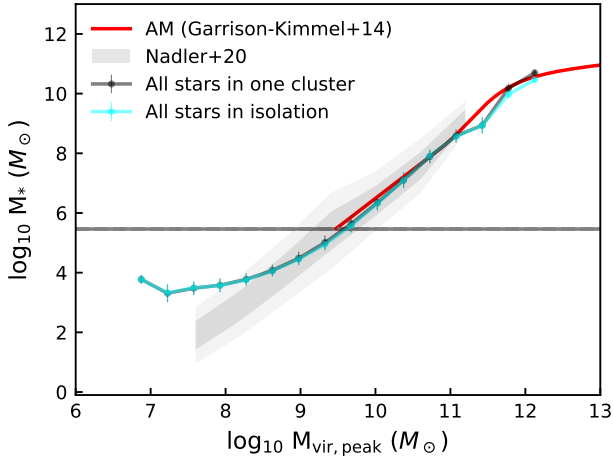


**Figure C1.** We show the SMHM relation from 30 *Caterpillar* trees if we assume that all massive stars reside in one big cluster in black and that all massive stars form in isolation in cyan.

stars reside in the very central region and can be considered as one cluster, and 2) all stars are in isolation. The resulting SMHM relations of these two cases are shown in Figure C1. The distinct difference lies in the most massive haloes, i.e., the MW in each *Caterpillar* tree. In such haloes, the number of massive stars is bigger and therefore the importance of  $\dot{M}_{\text{heat}}$  emerges.

#### APPENDIX D: DERIVATION OF $M_0$ IN MODEL F13

We show the derivation of Eq. 35 here. Following Bryan & Norman (1998), the mean density of a halo can be written as

$$\bar{\rho}_h = \frac{3M_{\text{vir}}}{4\pi r_{\text{vir}}^3} = \Delta_{\text{vir}} \rho_m(z) = \Delta_{\text{vir}} \Omega_m(z) \frac{3H^2(z)}{8\pi G}, \quad (\text{D1})$$

where  $M_{\text{vir}}$  is the virial mass of the halo,  $\Delta_{\text{vir}} = \bar{\rho}_h / \rho_m(z)$  is the over density,  $\Omega_m(z)$  is the redshift dependent matter density,  $H(z)$  is the Hubble constant, and  $G$  is the gravitational constant. We have the following equations:

$$\rho_m(z) = \Omega_m(z) \rho_c(z) = \rho_{m,0} (1+z)^3 = \Omega_{m,0} \frac{3H_0^2}{8\pi G} (1+z)^3, \quad (\text{D2})$$

and

$$r_{\text{vir}}^3 = h^{-2} M_{\text{vir}} \Delta_{\text{vir}}^{-1} \Omega_{m,0}^{-1} (1+z)^{-3} \frac{3}{4\pi} \frac{8\pi G}{3H_0^2}, \quad (\text{D3})$$

where  $H_0 = 67.8 \text{ kms}^{-1} \text{ Mpc}^{-1}$  (Planck Collaboration et al. 2016). We can rewrite Eq. D3 into

$$r_{\text{vir}} \simeq 210 h^{-1} \text{ kpc} \left( \frac{M_{\text{vir}}}{10^{12} h^{-1} M_{\odot}} \right)^{1/3} \times \left( \frac{\Delta_{\text{vir}}}{200} \right)^{-1/3} \Omega_{m,0}^{-1/3} (1+z)^{-1} \quad (\text{D4})$$

Therefore, the circular velocity at virial radius is

$$v_{\text{cir}} = \sqrt{\frac{GM_{\text{vir}}}{r_{\text{vir}}}} \simeq 146.6 \text{ kms}^{-1} \quad (\text{D5})$$

$$\left( \frac{M_{\text{vir}}}{10^{12} h^{-1} M_{\odot}} \right)^{1/3} \left( \frac{\Delta_{\text{vir}}}{200} \right)^{1/6} \Omega_{m,0}^{1/6} (1+z)^{1/2}$$

Finally, we have  $M_{\text{vir}}$  as a function of  $v_{\text{cir}}$ , over density  $\Delta_{\text{vir}}$ , and redshift  $z$ ,

$$\frac{M_{\text{vir}}}{10^{12} h^{-1} M_{\odot}} = \left( \frac{v_{\text{cir}}}{146.6 \text{ kms}^{-1}} \right)^3 \left( \frac{\Delta_{\text{vir}}}{200} \right)^{-1/2} \Omega_{m,0}^{-1/2} (1+z)^{-3/2}. \quad (\text{D6})$$

Here we assume that  $M_{\text{vir}}$  is at  $\Delta_{\text{vir}} = 200$  and substitute  $M_{\text{vir}} = M_0$  and  $v_{\text{cir}} = v_{\text{cool}}$  to arrive at Eq. 35.

This paper has been typeset from a  $\text{\TeX}/\text{\LaTeX}$  file prepared by the author.